JAGIELLONIAN UNIVERSITY
FACULTY OF PHYSICS, ASTRONOMY
AND APPLIED COMPUTER SCIENCE
INSTITUTE OF PHYSICS

A novel algorithm for the $K \to \pi^0\pi^0 \to \gamma\gamma\gamma\gamma$ decay vertex reconstruction for the KLOE-2 experiment

Aleksander Gajos

Master thesis
prepared in the Nuclear Physics Division
of the Jagiellonian University
supervised by

prof. dr hab. Paweł Moskal

and

dr Eryk Czerwiński

Cracow, 2013

Abstract

The aim of this work is to devise an auxiliary method of reconstruction of the $K \to \pi^0\pi^0$ decay vertex for the KLOE experiment. The requirement for reconstruction is not to depend on quantities that may be affected by kaon regeneration and thus to allow for its rejection as background for the $\phi \to K_S K_L \to \pi^+\pi^-\pi^0\pi^0$ process. A new reconstruction algorithm is proposed and implemented which uses four photons from the $K \to \pi^0\pi^0 \to \gamma\gamma\gamma\gamma$ decay chain recorded by an electromagnetic calorimeter and is based on finding their common origin point. A kinematic fit is included in the algorithm in order to tune the quantities used as input to vertex reconstruction and thus increase spatial resolution of vertex location. The final resolution achieved by the new reconstruction algorithm was found to be about 0.5 cm in each spatial coordinate for vertices of kaons decaying very close to their production point and about 2.5 cm for the most interesting region where the spherical beam pipe is present. The prospects of application of the new algorithm to rejection of regeneration background were tested in several ways.

Acknowledgements

I would like to express my deepest gratitude to my supervisors, prof. Paweł Moskal and dr Eryk Czerwiński, for their patience and the enormous effort they have put forth to introduce me to the KLOE experiment and to guide me throughout my work.

Moreover, I would like to thank prof. Bogusław Kamys for giving me the opportunity to work on my thesis in the Nuclear Physics Division of the Jagiellonian University.

I am also greatly indebted to prof. Antonio Di Domenico, dr Erika de Lucia and dr Antonio De Santis for their invaluable advice during our meetings and for making me feel at home in Frascati.

I am grateful to prof. Wojciech Wiślicki, dr Michał Silarski and dr Wojciech Krzemień for their suggestions that helped me solve numerous problems during my work.

I would like to thank my colleagues Izabela Pytko, Daria Kamińska, Krzysztof Kacprzak and the whole KLOE group from Cracow for the great and unique atmosphere in the group.

Finally, I express my cordial thanks to my family for their support and understanding they gave me when I was working on this thesis, and to my beloved Kasia Fornal — for everything.

I would also like to acknowledge the support of this work from the Foundation for Polish Science through the project HOMING PLUS BIS/2011-4/3,
as well as from the European Commission under the 7th Framework Programme through the 'Research Infrastructures' action of the 'Capacities' Programme,
Call: FP7-INFRASTRUCTURES-2008-1, Grant Agreement No. 283286.

Contents

Abstract iii

Acknowledgements v

1 Introduction 1

2 Neutral kaon physics 3
- 2.1 Neutral kaon states . . . 3
- 2.2 Kaon system properties . . . 5
- 2.3 Neutral kaon interferometry . . . 6
  - 2.3.1 Quantum entanglement of kaons . . . 6
  - 2.3.2 Measurement of $\frac{\epsilon'}{\epsilon}$ . . . 7
- 2.4 Kaon regeneration . . . 10

3 The DAΦNE collider and the KLOE experiment 13
- 3.1 The DAΦNE collider . . . 14
- 3.2 The KLOE detector . . . 15
  - 3.2.1 Geometry of the detector . . . 15
  - 3.2.2 Drift chamber . . . 16
  - 3.2.3 Electromagnetic calorimeter . . . 17
  - 3.2.4 Trigger . . . 20

4 The $\phi \to K_S K_L \to (K_S K_S \to)\pi^+\pi^-\pi^0\pi^0$ process at KLOE 23
- 4.1 Properties of the process . . . 24
- 4.2 Kaon regeneration at KLOE . . . 25
  - 4.2.1 Influence of regeneration on interferometric studies . . . 27
- 4.3 Standard $K_L \to \pi^0\pi^0$ reconstruction method . . . 28
  - 4.3.1 Principle of the reconstruction . . . 28
  - 4.3.2 Resolution of the method . . . 29
  - 4.3.3 Performance for events with regeneration . . . 31

5 New reconstruction method 33
- 5.1 Requirements . . . 33
- 5.2 Working principle . . . 34
- 5.3 Implementation of the method . . . 35
- 5.4 Method validity studies . . . 37
  - 5.4.1 Spatial resolution of the method for generated events . . . 37

5.4.2 Spatial resolution for reconstructed events 38
5.4.3 Influence of input data inaccuracy on spatial resolution 41

6 Tuning the input parameters 43
6.1 Fitting procedure 43
6.1.1 Principle of the fit 43
6.1.2 Tuned parameters and physical constraints 44
6.1.3 Minimization procedure 46
6.2 Results of input parameter tuning 49
6.3 Tuning the parameters with regeneration assumption 53

7 Application of the new reconstruction method 55
7.1 Rejection of regeneration events 55
7.1.1 Possibilities of regeneration recognition 55
7.2 Results 56

8 Conclusions 61

A Solution of the 4 spheres' intersection equation system 63

Bibliography 67

Chapter 1

Introduction

The K mesons were the first particles to be called *strange* by physicists due to a large difference in time scales between their production and decays which surprised scientists after their discovery in 1947 [1]. This was due to the fact that kaons contain the third lightest quark and so not only did the word *strange* permanently enter the scientific language as the name of the quark's flavour but also kaons with their peculiar properties become one of the most intensively examined particles in modern physics. Among them neutral kaons are of special interest as their observation led to the discovery of $\mathcal{CP}$ symmetry violation in 1964 [2]. Since then neutral K meson decays were studied in numerous experiments to examine both direct and indirect $\mathcal{CP}$ violation [3].

The neutral kaon system has, however, even more exciting properties to be examined. As flavoured mesons, kaons can be produced in pairs whose states are entangled in the sense of the Einstein-Podolsky-Rosen quantum correlation [4]. Moreover, the difference in masses of the two neutral kaons is small enough [5] for the interference phenomena resulting from the correlation to be measurable. This opens a new world for kaon interferometry, allowing for $\mathcal{CP}$ violation studies and even for tests of the basic quantum mechanics' principles such as the large-scale persistence of quantum coherence [6].

One of the possible interferometric studies with correlated kaon pairs involves the $\phi \to K_S K_L \to \pi^+\pi^-\pi^0\pi^0$ process in order to determine the $\frac{\epsilon'}{\epsilon}$ parameter which is a measure of the $\mathcal{CP}$ violation [7] (details on the neutral kaon physics are described in the next chapter). Here, however, kaons' peculiarities become both the friend and foe because the process of neutral kaon regeneration constitutes one of the major background sources in such an analysis. Regeneration is a transformation of one neutral kaon into the other one which destroys quantum correlation in the system while leading to the same final state as a signal event. In addition to the entanglement loss the regeneration taking place at the KLOE detection setup is predominantly incoherent [8] and changes the momentum direction of the kaon. This is especially difficult to recognize in case of the $K \to \pi^0\pi^0$ decay which

involves only neutral particles and therefore the momentum direction of the initial kaon cannot be precisely determined.

The KLOE experiment located in the National Nuclear Physics Laboratory in Frascati (Italy) was designed with a view to investigating the physics of kaon pairs produced in the ϕ meson decays among other studies such as η ans η' meson decays and search for the dark forces [9–11]. KLOE is a barrel-shaped detector located on the e^+e^- collider DAΦNE which operates at the energy equal to the ϕ meson resonance ($m_\phi = 1019.455 \pm 0.020$ MeV/c^2 [5]) leading to the ϕ meson production. The latter decays to two neutral kaons with a 34% branching fraction [5], thus providing numerous opportunities to observe correlated kaon pairs. A significant part of the long-lived K mesons, however, is regenerated while passing through elements of the detector. Moreover, the standard $K \to \pi^0\pi^0$ vertex reconstruction algorithm used in KLOE is not sensitive when incoherent regeneration happens, making it impossible to reject regeneration using vertex location. These facts raise a need for an auxiliary $K \to \pi^0\pi^0$ decay vertex reconstruction method which would not be prone to error in case of kaon regeneration and would provide means to recognize and efficiently reject such events.

This thesis presents a study on such a new reconstruction algorithm developed and tested with a view to its application as a tool for regeneration background rejection for the data collected by the KLOE experiment and for further usage in the KLOE-2 experiment. The work is divided into eight chapters. Chapter 2 describes basic properties of the neutral kaon system and the neutral kaon regeneration mechanism as well as the quantum entanglement phenomenon with its use for interferometric studies. These are followed by a detailed description of the DAΦNE collider and the KLOE experiment in Chapter 3. Chapter 4 presents the $\phi \to \mathrm{KK} \to \pi^+\pi^-\pi^0\pi^0$ process as well as the standard method of $K \to \pi^0\pi^0$ vertex reconstruction and its sensitivity to the regeneration process. Chapter 5 comprises the operation principle and implementation details of the new reconstruction algorithm, followed by its tests. Chapter 6 is devoted to the details of a fit method introduced to increase reconstruction accuracy. Finally, results of application of the new method to regeneration background rejection in the KLOE data are contained in Chapter 7, leading to the conclusions summarized in the last chapter.

Chapter 2

Neutral kaon physics

Being the first observed particles that contain the strange quark, kaons gave rise to the new field of flavour physics with phenomena inaccessible using unflavoured particles. Additionally, because of their relatively small mass (m_K =497.614±0.024 MeV/c^2 [5]) they are easily produced at medium energy range accelerators and thus have been studied in numerous experiments through last decades (NA31, NA48, KTeV [12–14] are only a few examples) which contributed to understanding of such fundamental issues as the $\mathcal{CP}$ symmetry and its violation.

One of the most interesting experimental techniques available with kaons is the neutral kaon interferometry which utilizes the quantum entanglement in neutral kaon pairs allowing for various measurements as the simultaneous determination of direct and indirect $\mathcal{CP}$ violation observables [15]. However, an obstacle to such investigations is the regeneration process, inevitable in neutral K meson systems.

This chapter starts with the description of neutral kaon states well-defined at their production and decays as well as the properties of decaying states which will be useful for further considerations. Furthermore, the mechanism of quantum entanglement is presented followed by its application to determine the $\frac{\epsilon'}{\epsilon}$ parameter in the study of $K_S K_L \to \pi^+\pi^-\pi^0\pi^0$ channel. Finally, the regeneration process is explained as well as its impact on the feasibility of the interferometric investigations.

2.1 Neutral kaon states

Kaons are light pseudoscalar mesons containing the strange quark and therefore have a non-zero strangeness quantum number. The four K mesons constitute two isospin doublets: (K^+, K^0) with S=1 and (K^-, $\overline{K}^0$) with S=-1. Table 2.1 presents the quark content of kaons. The two neutral, K^0 and its antiparticle $\overline{K}^0$, will be discussed in more detail as their properties are of great importance to this work.

	K^+	K^-	K^0	$\overline{K}^0$
quarks	$u\bar{s}$	$\bar{u}s$	$d\bar{s}$	$\bar{d}s$
strangeness	1	-1	1	-1

TABLE 2.1: Quark content and strangeness of the K mesons.

Strangeness is conserved in strong interactions through which kaons are produced and thus their creation from non-strange particles requires that they either appear in pairs or along with another strange particle like Λ^0 ($\Lambda^0 = uds$). Strangeness conservation makes the basis of strangeness operator eigenstates suitable for describing the production of kaons. Their decays, however, occur through weak processes where strangeness is not conserved and a different basis is necessary for a convenient description of the decaying states.

Let us consider a basis of states with well-defined $\mathcal{CP}$ values. Although K^0 and $\overline{K}^0$ are clearly not $\mathcal{CP}$ eigenstates:

$$\mathcal{CP}\,|K^0\rangle = |\overline{K}^0\rangle\,, \quad \mathcal{CP}\,|\overline{K}^0\rangle = |K^0\rangle\,,$$

their linear combinations can be used to construct a proper $\mathcal{CP}$ basis:

$$\begin{aligned} |K_1^0\rangle &= \frac{1}{\sqrt{2}}\left(|K^0\rangle + |\overline{K}^0\rangle\right) \qquad \mathcal{CP} = +1, \\ |K_2^0\rangle &= \frac{1}{\sqrt{2}}\left(|K^0\rangle - |\overline{K}^0\rangle\right) \qquad \mathcal{CP} = -1. \end{aligned} \tag{2.1}$$

The K_1^0 and K_2^0 states can be identified as the decaying kaons. Since they decay mostly into pions, for $\mathcal{CP}$ symmetry to hold, K_1^0 may only decay into two pions whereas for the K_2^0 decay only a three-pion final state is possible. The K_1^0 and K_2^0 states are often called short and long-lived (K_S, K_L), respectively, because a more limited phase space for the $K_2^0 \to 3\pi$ decay makes its life time significantly larger than K_1^0.

Kaon decays, however, involve weak interactions which violate the $\mathcal{CP}$ symmetry as it was proven in 1964 by Christenson, Cronin, Fitch and Turlay in their experiment [2]. They observed a decay of the long-lived kaon into $\pi^+\pi^-$ with a branching fraction of the order of 10^{-3} and thus neutral K mesons have provided the first evidence of $\mathcal{CP}$ symmetry violation in weak interactions. It is then apparent that the decaying kaon states are not well-defined $\mathcal{CP}$ eigenstates.

In order to account for possible $\mathcal{CP}$ violation, the K_1^0 and K_2^0 states from Eq. 2.1 have to be corrected by introducing small parameters ϵ_S and ϵ_L:

$$\begin{aligned} |K_S\rangle &= \frac{1}{\sqrt{2(1+|\epsilon_S|^2)}}\left((1+\epsilon_S)\left|K^0\right\rangle + (1-\epsilon_S)\left|\overline{K}^0\right\rangle\right), \\ |K_L\rangle &= \frac{1}{\sqrt{2(1+|\epsilon_L|^2)}}\left((1+\epsilon_L)\left|K^0\right\rangle - (1-\epsilon_L)\left|\overline{K}^0\right\rangle\right). \end{aligned} \tag{2.2}$$

The above states properly describe the decaying kaons and are labelled K_S and K_L for *short-lived* and *long-lived* kaon, respectively. They are also eigenstates of the effective hamiltonian **H** of the neutral kaon system which includes strong and electromagnetic as well as weak interactions. Although the effective hamiltonian is not hermitian, it can be decomposed into hermitian and anti-hermitian parts (in the $\{K^0, \overline{K}^0\}$ basis) [6]:

$$\mathbf{H} = \begin{pmatrix} H_{11} & H_{12} \\ H_{21} & H_{22} \end{pmatrix} = \mathbf{M} - \frac{i}{2}\mathbf{\Gamma} = \begin{pmatrix} M_{11} & M_{12} \\ M_{12}^* & M_{22} \end{pmatrix} - \frac{i}{2}\begin{pmatrix} \Gamma_{11} & \Gamma_{12} \\ \Gamma_{12}^* & \Gamma_{22} \end{pmatrix}. \tag{2.3}$$

The eigenvalues of **H** corresponding to eigenstates $\{K_S, K_L\}$ are then:

$$\begin{aligned} \lambda_S &= m_S - i\frac{\Gamma_S}{2}, \\ \lambda_L &= m_L - i\frac{\Gamma_L}{2}. \end{aligned} \tag{2.4}$$

2.2 Kaon system properties

Basic properties and most important decay channels of the long-lived and short-lived kaon states are given in Table 2.2. Further in this work, only the decay channels into two pions

	K_S		K_L	
mean life time	(89.54 ± 0.04) ps		(51.16 ± 0.21) ns	
mass	(497.614 ± 0.024) MeV/c^2			
mass difference	(3.484 ± 0.006)×10^{-12} MeV/c^2			
major decay modes (branching ratio)	$\pi^+\pi^-$	(6.920 ± 0.005)×10^{-1}	$\pi^\pm e^\mp \nu_e$	(4.055 ± 0.011)×10^{-1}
	$\pi^0\pi^0$	(3.069 ± 0.005)×10^{-1}	$\pi^\pm \mu^\mp \nu_\mu$	(2.704 ± 0.007)×10^{-1}
	$\pi^+\pi^-\gamma$	(1.79 ± 0.05) ×10^{-3}	$3\pi^0$	(1.952 ± 0.012)×10^{-1}
	$\pi^\pm e^\mp \nu_e$	(7.04 ± 0.08) ×10^{-4}	$\pi^+\pi^-\pi^0$	(1.254 ± 0.005)×10^{-1}
	$\pi^\pm \mu^\mp \nu_\mu$	(4.69 ± 0.05) ×10^{-4}	$\pi^\pm e^\mp \nu_e \gamma$	(3.79 ± 0.06) ×10^{-3}
			$\pi^+\pi^-$	(1.966 ± 0.010) ×10^{-3}
			$\pi^0\pi^0$	(8.64 ± 0.06) ×10^{-4}

TABLE 2.2: Some of the properties and decay modes of neutral kaons [5].

will be considered. Therefore it is worth noting that whereas K_S predominantly decays into two pions, for K_L similar decays violate the $\mathcal{CP}$ symmetry and thus are much less probable than semileptonic and three-pion decay modes. Furthermore, as it was mentioned in the introduction to this chapter, the fact that mass difference between short and long-lived kaons is small is crucial for the possibility of interference phenomena observation on measurable time scales.

2.3 Neutral kaon interferometry

2.3.1 Quantum entanglement of kaons

When kaons are produced in the decays of unflavoured neutral mesons, strangeness conservation demands that they are created in pairs. Moreover, as the decays are strong, $\mathcal{C}$ and $\mathcal{P}$ values of the original meson must also be preserved. For instance, in the decay of a ϕ meson with $\mathrm{J}^{PC} = 1^{--}$ into two neutral kaons, the simplest state of the kaon system which is an eigenstate of both $\mathcal{C}$ and $\mathcal{P}$ with eigenvalues equal to -1 can be constructed as a linear superposition of zero-strangeness states [6]:

$$|i\rangle = \frac{1}{\sqrt{2}} \left(\left|\mathrm{K}^0(+\vec{p})\right\rangle \left|\overline{\mathrm{K}}^0(-\vec{p})\right\rangle - \left|\overline{\mathrm{K}}^0(+\vec{p})\right\rangle \left|\mathrm{K}^0(-\vec{p})\right\rangle \right), \tag{2.5}$$

where the momenta of kaons are expressed in the center of mass (CM) reference frame. The state is labelled $|i\rangle$ as the initial state of the neutral kaon system produced in a ϕ decay.

As mentioned before, kaon decays are described more conveniently in the $\{\mathrm{K_S}, \mathrm{K_L}\}$ basis, therefore for further considerations, based on equations (2.2), equation (2.5) can be transformed into:

$$|i\rangle = \frac{\mathcal{N}}{\sqrt{2}} \left(|\mathrm{K}_S(+\vec{p})\rangle \, |\mathrm{K}_L(-\vec{p})\rangle - |\mathrm{K}_L(+\vec{p})\rangle \, |\mathrm{K}_S(-\vec{p})\rangle \right) \tag{2.6}$$

with:

$$\mathcal{N} = \frac{\sqrt{(1+|\epsilon_S|^2)(1+|\epsilon_L|^2)}}{1-\epsilon_S\epsilon_L} \simeq 1$$

as a normalization factor.

Let us now assume that the two neutral kaons decay into two final states f_1, f_2 after their proper times t_1 and t_2, respectively, and let $\mathbf{T}$ denote the transition matrix. The time-dependent amplitude of the $f_1 f_2$ final state is then of the form:

$$A(f_1, t_1; f_2, t_2) = \frac{\mathcal{N}}{\sqrt{2}} \big(\langle f_1|\mathbf{T}|\mathrm{K_S}(t_1)\rangle \, \langle f_2|\mathbf{T}|\mathrm{K_L}(t_2)\rangle - \langle f_1|\mathbf{T}|\mathrm{K_L}(t_1)\rangle \, \langle f_2|\mathbf{T}|\mathrm{K_S}(t_2)\rangle \big) \tag{2.7}$$

The time evolution of K_S and K_L states is given by [6]:

$$\begin{aligned} |\mathrm{K}_S(t)\rangle &= e^{-\lambda_S t} \, |\mathrm{K}_S\rangle = e^{-(m_S - \frac{\Gamma_S}{2})t} \, |\mathrm{K}_S\rangle \,, \\ |\mathrm{K}_L(t)\rangle &= e^{-\lambda_L t} \, |\mathrm{K}_L\rangle = e^{-(m_L - \frac{\Gamma_L}{2})t} \, |\mathrm{K}_L\rangle \,. \end{aligned} \tag{2.8}$$

Inserting it into the amplitude (2.7) and taking the square yields the probability of kaons decaying to a $f_1 f_2$ final state in times t_1 and t_2:

$$\begin{aligned} I(f_1, t_1; f_2, t_2) = C_{12}\Big[&|\eta_1|^2 e^{-\Gamma_L t_1 - \Gamma_S t_2} + |\eta_2|^2 e^{-\Gamma_S t_1 - \Gamma_L t_2} \\ &- 2|\eta_1||\eta_2| e^{\frac{\Gamma_S + \Gamma_L}{2}(t_1+t_2)} \cos(\Delta m(t_1 - t_2) + \varphi_2 - \varphi_1)\Big] \end{aligned} \tag{2.9}$$

where

$$C_{12} = \frac{|\mathcal{N}|^2}{2} |\langle f_1 \,|\, \mathbf{T} \,|\, \mathrm{K_S}\rangle \langle f_2 \,|\, \mathbf{T} \,|\, \mathrm{K_S}\rangle|^2,$$

η_i are defined as ratios of transition amplitudes:

$$\eta_i = \frac{\langle f_i \,|\, \mathbf{T} \,|\, \mathrm{K_L}\rangle}{\langle f_i \,|\, \mathbf{T} \,|\, \mathrm{K_S}\rangle}, \tag{2.10}$$

φ_i are their respective complex phases and Δm is the mass difference between $\mathrm{K_S}$ and $\mathrm{K_L}$ (see Section 2.2).

The interference term in the second line of expression (2.9) describes the quantum correlation of $\mathrm{K_S}$ and $\mathrm{K_L}$ states produced in the same ϕ decay. Indeed, in the initial state of the neutral kaon system (2.6) none of the two kaons' states can be expressed independently of the other one. This phenomenon was first described by Einstein, Podolsky and Rosen in their famous work [4] as a paradox in quantum mechanics. If one of two particles in such a superposition of states is measured for a certain observable, this immediately implies knowledge of this observable for the second particle regardless of their spatial separation.

Interferometric investigations with the neutral kaon system allow for testing quantum mechanics principles from which these large-scale correlations result, but the presence of the interference term also allows for numerous other measurements such as the simultaneous determination of the real and imaginary part of the $\mathcal{CP}$ violation parameter $\frac{\epsilon'}{\epsilon}$, which will be described in the following section.

2.3.2 Measurement of $\frac{\epsilon'}{\epsilon}$

The coefficients ϵ_S, ϵ_L from equation (2.2) which describe the degree of $\mathcal{CP}$ violation in $\mathrm{K_S}$ and $\mathrm{K_L}$ mesons may also be parametrized as [6]:

$$\bar{\epsilon} = \frac{\epsilon_S + \epsilon_L}{2}, \qquad \delta = \frac{\epsilon_S - \epsilon_L}{2},$$

where $\bar{\epsilon}$ can be defined using elements of the hamiltonian of neutral kaon system (2.3) after neglecting higher order terms [16]:

$$\bar{\epsilon} = \frac{\mathrm{H_{12}} - \mathrm{H_{21}}}{2(\lambda_S - \lambda_L)}.$$

As the equality of effective hamiltonian elements $\mathrm{H}_{12} = \mathrm{H}_{21}$ should hold if the $\mathcal{CP}$ symmetry is conserved, the value of $\overline{\epsilon}$ is a measure of $\mathcal{CP}$ violation. This parameter is, however, dependent on the phase convention [16]. Fortunately, there are also several other ways to define the two $\mathcal{CP}$ violation parameters which are independent of the phase convention. In this work a definition sometimes referred to as "experimental" will be used as in [17, 18], and a comprehensive summary of other possible approaches can be found in [19].

Let us consider the transition amplitudes of kaons as isospin states into two-pion final states with definite isospin value I:

$$\begin{aligned} \langle \pi\pi(I)|\mathbf{T}|\mathrm{K}^0\rangle &= A_I e^{i\delta_I}, \\ \langle \pi\pi(I)|\mathbf{T}|\overline{\mathrm{K}}^0\rangle &= \overline{A}_I e^{i\delta_I}. \end{aligned} \tag{2.11}$$

As only final states with $I = 0$ or 2 are possible, amplitudes of decays of the $\mathrm{K_S}$ and $\mathrm{K_L}$ states into $\pi^0\pi^0$ and $\pi^+\pi^-$ can be expressed in terms of A_0 and A_2 and the respective η_i parameters (2.10) may be decomposed into the following combinations [18]:

$$\begin{aligned} \eta_{00} &= \frac{\langle \pi^0\pi^0|\mathbf{T}|\mathrm{K_L}\rangle}{\langle \pi^0\pi^0|\mathbf{T}|\mathrm{K_S}\rangle} = \epsilon - 2\epsilon', \\ \eta_{+-} &= \frac{\langle \pi^+\pi^-|\mathbf{T}|\mathrm{K_L}\rangle}{\langle \pi^+\pi^-|\mathbf{T}|\mathrm{K_S}\rangle} = \epsilon + \epsilon' \end{aligned} \tag{2.12}$$

of parameters ϵ, ϵ' which (after neglecting higher order terms) are given as:

$$\begin{aligned} \epsilon &= \overline{\epsilon} + i\frac{\Im(A_0)}{\Re(A_0)}, \\ \epsilon' &= i\frac{e^{i(\delta_2-\delta_0)}}{\sqrt{2}}\frac{\Re(A_2)}{\Re(A_0)}\left[\frac{\Im(A_2)}{\Re(A_2)} - \frac{\Im(A_0)}{\Re(A_0)}\right]. \end{aligned} \tag{2.13}$$

The above parameters are measurable and independent of the phase convention. A non-zero value of ϵ' indicates direct $\mathcal{CP}$ violation whereas ϵ is a measure of indirect $\mathcal{CP}$ violation [18].

Based on the branching fractions of neutral kaon decays into two-pion final states it is possible to determine the real part of the ϵ'/ϵ ratio using the relation [19]:

$$\Re\left(\frac{\epsilon'}{\epsilon}\right) \simeq \frac{1}{6}\left(1 - \left|\frac{\eta_{00}}{\eta_{+-}}\right|^2\right). \tag{2.14}$$

The average result of such a measurement is [5]:

$$\Re\left(\frac{\epsilon'}{\epsilon}\right) = (1.66 \pm 0.23) \times 10^{-3}. \tag{2.15}$$

It is worth to note that it is impossible to probe $\Im\left(\frac{\epsilon'}{\epsilon}\right)$ in a similar manner. This is where interferometic methods reveal their potential, as the study of correlation between decays

in the $K_S K_L \to \pi^+\pi^-\pi^0\pi^0$ process allows for a simultaneous measurement of both the real and imaginary part of $\frac{\epsilon'}{\epsilon}$.

In Section 2.3.1 the probability of a neutral kaon system decaying into final states f_1, f_2 in times t_1, t_2 was derived. The two final states may be chosen as $f_1 = \pi^+\pi^-$ and $f_2 = \pi^0\pi^0$. Moreover, if equation (2.9) is integrated over $t_1 + t_2$ with fixed $\Delta t = t_1 - t_2$, a formula is obtained for the probability of the decays taking place with a certain time difference rather that in absolute times [6]:

$$\begin{aligned} I_{+-00}(\Delta t \geq 0) = I(\pi^+\pi^-, \pi^0\pi^0; \Delta t) = \frac{C_{12}}{\Gamma_s + \Gamma_L}\Big[|\eta_{+-}|^2 e^{-\Gamma_L \Delta t} + |\eta_{00}|^2 e^{-\Gamma_S \Delta t} \\ - 2|\eta_{+-}||\eta_{00}| e^{\frac{\Gamma_S+\Gamma_L}{2}\Delta t}\cos(\Delta m \Delta t + \varphi_2 - \varphi_1)\Big] \end{aligned} \tag{2.16}$$

Although the above is valid only for $\Delta t \geq 0$, a symmetrical formula is obtained for $\Delta t < 0$ by exchanging the f_1 and f_2 states. Figure 2.1 shows a complete plot of the I_{+-00} probability as a function of Δt. The time difference is expressed in units of K_S lifetime for convenience. It can be seen that the non-zero value of the $\frac{\epsilon'}{\epsilon}$ parameter results in an asymmetry of this distribution around $\Delta t = 0$.

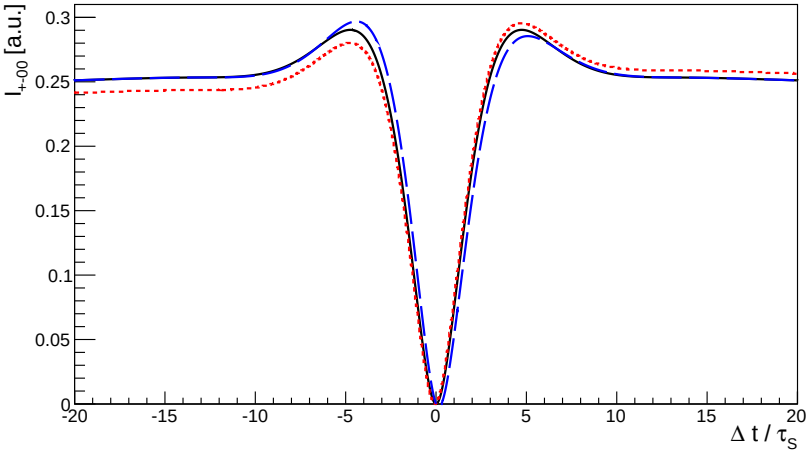

FIGURE 2.1: Intensity of $\phi \to K_S K_L \to \pi^+\pi^-\pi^0\pi^0$ decays $I_{+-00}(\Delta t)$ as a function of the difference of kaon decay times. Solid (black) line corresponds to $\frac{\epsilon'}{\epsilon} = 0$, dotted (red) line to $\Re\left(\frac{\epsilon'}{\epsilon}\right) = 0.01$ and dashed (blue) line to $\Im\left(\frac{\epsilon'}{\epsilon}\right) = 0.05$. The region $|\Delta t/\tau_S| < 5$ is sensitive to $\Im\left(\frac{\epsilon'}{\epsilon}\right)$ while for large $|\Delta t/\tau_S|$ the intensity asymmetry tends to $3\Re\left(\frac{\epsilon'}{\epsilon}\right)$.

In order to measure this asymmetry the following time-dependent asymmetry function is introduced:

$$A_{\epsilon'/\epsilon}(|\Delta t|) = \frac{I_{+-00}(\Delta t > 0) - I_{+-00}(\Delta t < 0)}{I_{+-00}(\Delta t > 0) + I_{+-00}(\Delta t < 0)}. \tag{2.17}$$

This function can be separated into components proportional to $\Re\left(\frac{\epsilon'}{\epsilon}\right)$ and $\Im\left(\frac{\epsilon'}{\epsilon}\right)$ [17]:

$$A_{\epsilon'/\epsilon}(|\Delta t|) = A_R(|\Delta t|)\Re\left(\frac{\epsilon'}{\epsilon}\right) - A_I(|\Delta t|)\Im\left(\frac{\epsilon'}{\epsilon}\right), \tag{2.18}$$

where

$$\begin{aligned} A_R(|\Delta t|) &= 3\frac{e^{-\Gamma_L|\Delta t|} - e^{-\Gamma_S|\Delta t|}}{e^{-\Gamma_L|\Delta t|} + e^{-\Gamma_S|\Delta t|} - 2e^{-\frac{\Gamma_L+\Gamma_S}{2}|\Delta t|}\cos(\Delta m|\Delta t|)} \\ A_I(|\Delta t|) &= 3\frac{2e^{-\frac{\Gamma_L+\Gamma_S}{2}|\Delta t|}\sin(\Delta m|\Delta t|)}{e^{-\Gamma_L|\Delta t|} + e^{-\Gamma_S|\Delta t|} - 2e^{-\frac{\Gamma_L+\Gamma_S}{2}|\Delta t|}\cos(\Delta m|\Delta t|)}. \end{aligned} \tag{2.19}$$

An important result of (2.19) is that $A_{\epsilon'/\epsilon}$ is sensitive to the $\Re\left(\frac{\epsilon'}{\epsilon}\right)$ and $\Im\left(\frac{\epsilon'}{\epsilon}\right)$ parameters for distinct ranges of the time difference. It can be shown [15] that:

$$A_{\epsilon'/\epsilon} \xrightarrow{|\Delta t \gg \tau_S|} 3\Re\left(\frac{\epsilon'}{\epsilon}\right), \tag{2.20}$$

whereas for $|\Delta t| < 5\tau_S$ the asymmetry is sensitive to $\Im\left(\frac{\epsilon'}{\epsilon}\right)$.

The simultaneous extraction of the real and imaginary parts of $\frac{\epsilon'}{\epsilon}$ is possible by means of a fit of the asymmetry function (2.19) to the asymmetry calculated from an experimental distribution of $I_{+-}(\Delta t)$. The latter can be determined in an experiment where entangled neutral kaon pairs are produced and their decay times can be measured.

2.4 Kaon regeneration

Neutral kaon regeneration is a peculiar process leading to the fact that when an initially-pure beam of $\mathrm{K_S}$ or $\mathrm{K_L}$ traverses through matter, a non-zero component of the other state appears in the beam. Predicted theoretically by Pais and Piccioni in 1955 [20], it was observed in experiment 6 years later and used as a tool to determine the mass difference between $\mathrm{K_S}$ and $\mathrm{K_L}$ [21].

Regeneration results from the mass eigenstates of kaons ($\mathrm{K_S}$, $\mathrm{K_L}$) being superpositions of K^0 and $\overline{\mathrm{K}}^0$ as in (2.2). K mesons passing through matter can undergo strong interactions with nucleons which are well described in the $\{\mathrm{K}^0, \overline{\mathrm{K}}^0\}$ basis. However, it turns out that the conservation of quantum numbers does not allow the same set of reactions for K^0 and $\overline{\mathrm{K}}^0$. For instance, the processes:

$$\begin{aligned} \overline{\mathrm{K}}^0 + \mathrm{p} &\to \Lambda^0 + \pi^+, \\ \overline{\mathrm{K}}^0 + \mathrm{n} &\to \Lambda^0 + \pi^0 \end{aligned}$$

have no equivalent for K^0. As a result, the total cross section for interaction with nucleons is larger for $\overline{\mathrm{K}}^0$ than for K^0 (except for the asymptotic region where equality holds) [22]:

$$\sigma_T(\overline{\mathrm{K}}^0\mathrm{N}) \geq \sigma_T\left(\mathrm{K}^0\mathrm{N}\right). \tag{2.21}$$

Let us now consider the evolution of a beam of pure $\mathrm{K_L}$ state traversing through matter. The initial state can be expressed as:

$$|i\rangle = |\mathrm{K_L}\rangle = \frac{1}{\sqrt{1-|\epsilon_L|^2}}\left((1+\epsilon_L)\left|\mathrm{K}^0\right\rangle - (1-\epsilon_L)\left|\overline{\mathrm{K}}^0\right\rangle\right), \tag{2.22}$$

and the final state $|f\rangle$ after the interaction may be described using the angle-dependent scattering amplitudes $f(\theta)$ and $\overline{f}(\theta)$ for K^0 and $\overline{\mathrm{K}}^0$ respectively:

$$|f\rangle = \frac{1}{\sqrt{1-|\epsilon_L|^2}}\left(f(\theta)(1+\epsilon_L)\left|\mathrm{K}^0\right\rangle - \overline{f}(\theta)(1-\epsilon_L)\left|\overline{\mathrm{K}}^0\right\rangle\right). \tag{2.23}$$

When the transition back to the $\{\mathrm{K_S}, \mathrm{K_L}\}$ basis is made it becomes apparent that a component of the $\mathrm{K_S}$ state may appear in the initially-pure $\mathrm{K_L}$ beam if the scattering amplitudes differ:

$$|f\rangle = \frac{f(\theta)+\overline{f}(\theta)}{2}|\mathrm{K_L}\rangle + \frac{f(\theta)-\overline{f}(\theta)}{2}|\mathrm{K_S}\rangle. \tag{2.24}$$

The difference of scattering amplitudes is indeed non-zero as a result of (2.21). Therefore it is useful to define the regeneration amplitude using this difference [22]:

$$f_{reg}(\theta) \equiv \frac{f(\theta)-\overline{f}(\theta)}{2}. \tag{2.25}$$

Value of $f_{reg}(\theta)$ depends on the type of the regeneration process which can be coherent or incoherent due to different possible ways of scattering in the medium [8]. In coherent regeneration the kaon does not change its direction ($\theta < 10^{-6}$ rad) whereas the incoherent (elastic) regeneration results in a change of the momentum direction of the kaon with a probability dependent on the regeneration angle θ. A detailed analysis of these two kinds of regeneration and their probabilities can be found in ref. [8, 22].

Neutral kaon regeneration is an important obstacle in the interferometric studies described in the previous section which are performed for example at the KLOE experiment. Next chapter gives a description of the KLOE experimental setup as well as an overview of regeneration possible in that case.

Chapter 3

The DAΦNE collider and the KLOE experiment

The KLOE Experiment is situated at the DAΦNE e^+e^- collider [23] in the National Laboratory of Frascati (LNF) which is a part of the Italian National Institute for Nuclear Physics (INFN) located in the city of Frascati near Rome. The idea of building a ϕ-factory was born in 1989 [24] and only two years later the construction of a sophisticated detector was proposed for studying $\mathcal{CP}$ violation in the system of neutral kaons.

KLOE started its operation in 1999 and was taking data during two periods — in the years 2001–2002 and 2004–2005. A total of about 2.5 fb^{-1} of data was collected which corresponds to about 10^{10} of ϕ mesons produced. Presently an upgrade of KLOE is being performed with a view to starting the new generation of experiment — KLOE-2 which aims at both higher precision and luminosity (DAΦNE has already proved its capability of delivering a luminosity 3 times higher than before the upgrade [25]).

The name of KLOE stands for the *K-LOng Experiment* and indeed multiple traits of its setup are dictated exclusively by the special properties of the long-lived neutral kaon such as its unusually long lifetime and the possibility of regeneration.

This chapter is started with a description of the DAΦNE collider as the source of ϕ mesons for KLOE. Subsequently, an overview of the KLOE detector is presented followed by details of its two major components — the drift chamber and the electromagnetic calorimeter. A particular emphasis is put on the latter as it is the source of information used in the reconstruction algorithm presented in this work, and its properties are of special importance for future considerations.

3.1 The DAΦNE collider

As it is indicated by its full name which stands for *Double Annular Factory for Nice Experiments*, the DAΦNE collider is composed of two separate storage rings as shown in the right side of Figure 3.1. Such design allows for a larger number of bunches in the rings in comparison to the conventional single-ring colliders, thus leading to a higher luminosity. Each ring of DAΦNE stores a beam of the energy of 0.51 GeV composed of 120 bunches of particles — electrons in one of them and positrons in the other. A single bunch is a packet of about 8.9×10^{10} particles which collides with a bunch of its antiparticles once per cycle [23, 24].

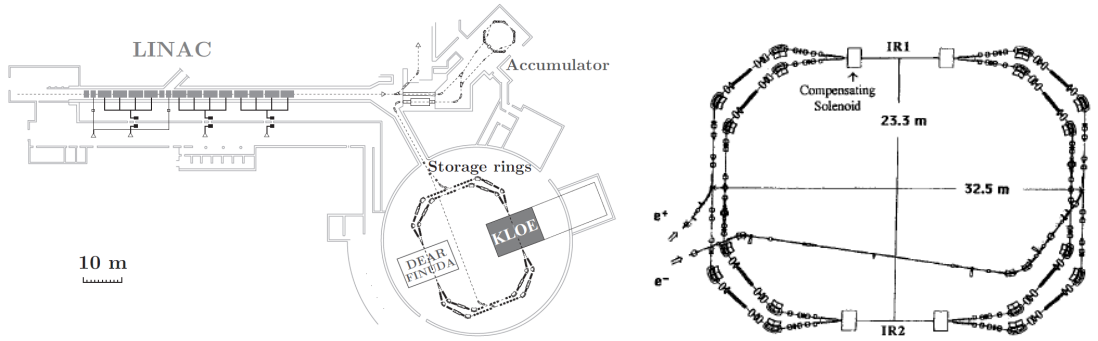

FIGURE 3.1: The accelerator complex at LNF (left) and the DAΦNE storage rings (right). On the left figure the location of the KLOE experiment on one of two interaction regions of DAΦNE is also presented. The figures are adapted from [24] and [23] respectively.

In order to compensate for the decaying intensities of stored beams, several times per hour the rings are injected with new particles produced in the accelerator complex (Figure 3.1, left). The LINAC produces electrons which are either directly transferred to the accumulator or used to produce positrons on a metallic target. The accumulator is then used for both electrons and positrons to reduce the emittances of the initial LINAC beam and to form a bunch which is finally injected into the ring.

There are two intersection points at the rings where the beams collide at an angle of $(\pi - 0.025)$ rad which is a result of the double-ring design. Since both rings lie in one horizontal plane, the beam horizontal size is defined very well whereas the transverse and longitudinal ones are larger by orders of magnitude. Mean beam sizes are shown in Table 3.1 along with other DAΦNE parameters.

The beam energy is chosen so that the canter-of-mass energy of the colliding e^+e^- system is at the peak of the ϕ meson, that is $\sqrt{s} \simeq m_\phi = 1019.45$ MeV. Thus in the collisions the ϕ meson is predominantly produced with a peak cross section of about 3 μb^{-1} which is the reason for DAΦNE being called a ϕ-factory.

The collision energy close to the peak results in the ϕ meson being produced almost at rest (with $\beta_\phi \approx 0.015$) in the laboratory frame although it has a small momentum component

beam energy		510 MeV
bunches per beam		120
particles per bunch		8.9×10^{10}
bunch size	σ_x	0.02 cm
	σ_y	0.002 cm
	σ_z	3 cm
max. luminosity		$5\times10^{32}\ cm^{-2}s^{-1}$
RF frequency		368.25 MHz

TABLE 3.1: Selected parameters of the DAΦNE collider [23].

towards the center of the storage rings due to the beam crossing geometry. The ϕ meson decays almost immediately ($\tau_\phi = 1.55 \pm 0.01 \times 10^{-22}$ s [5]) through strong interaction, mostly producing kaon pairs. Table 3.2 contains a summary of major ϕ decay channels.

Decay channel	branching ratio [%]
$\phi \to \mathrm{K^+K^-}$	48.9±0.5
$\phi \to \mathrm{K_S K_L}$	34.2±0.4
$\phi \to \rho\pi^0, \phi \to \pi^+\pi^-\pi^0$	15.32±0.32
$\phi \to \eta\gamma$	1.309±0.024

TABLE 3.2: Main decay channels of the ϕ meson [5].

3.2 The KLOE detector

3.2.1 Geometry of the detector

KLOE, installed at Interaction Region 1 of DAΦNE (Figure 3.1, right), is a detector of a barrel geometry surrounding the point of the e^+e^- collisions and covering 98% of the full solid angle. Figure 3.2 shows a cross section of the detector in the plane of beam axis and vertical direction. The two basic components of KLOE are the drift chamber (DC) and the electromagnetic calorimeter (EMC). The latter is constituted by the barrel part with an inner radius of 2 m and two endcaps mounted at the barrel ends which altogether enclose the volume of the detector. The drift chamber is a cylinder of a 2 m outer radius and inner radius of 25 cm filling all the space allowed by the EMC and by the focusing quadrupole magnets mounted on the beam pipe. The sensitive detector components are surrounded by a superconducting coil which provides a magnetic field of 0.52 T along the beam axis.

The large size of KLOE is necessary for the possibility of recording decays of the K_L meson. The mean path of a long-lived kaon in KLOE is about 3.4 m even despite its small velocity ($\beta_K \approx 0.22$) and therefore a large fiducial volume is necessary for capturing a reasonable number of its decays. KLOE with its dimensions is able to record decays of about 40% of the produced $\mathrm{K_L}$ mesons.

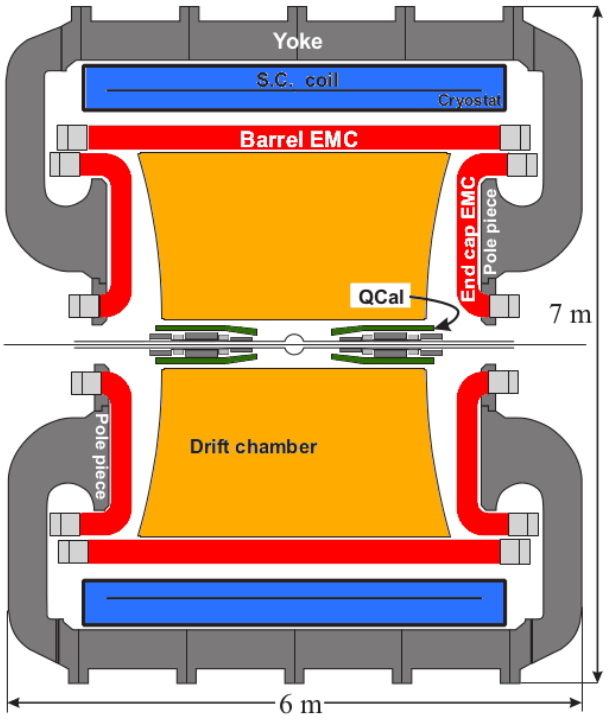

FIGURE 3.2: Cross section of the KLOE detector. The drift chamber (orange) is a cylindrical shape surrounding the interaction point. Two quadrupole magnets mounted on the beam pipe are covered with additional QCAL calorimeters [26] (green). The electromagnetic calorimeter (red) consists of a barrel part surrounding the drift chamber and the two end caps which close the barrel. The whole setup is immersed in magnetic field provided by a superconductiong coil (blue) located around the calorimeter barrel. The figure is adapted from [24].

For the system of coordinates used at the KLOE the geometrical middle point of the beam pipe at the interaction region is chosen as (0,0,0). The x axis points radially towards the outside of DAΦNE in the horizontal plane, y is the vertical direction pointing upwards and the z axis lies along the intersection of the angle between the crossing beams in the direction positrons' movement [24]. This coordinate system will be used in the remainder of this work.

3.2.2 Drift chamber

Tracking and identification of charged particles in KLOE is performed by a drift chamber being one of the largest of such devices ever constructed [27]. It contains a total of about 52000 wires aligned to the chamber axis between its end plates. About 12500 of the wires are collecting the charge deposited by an ionizing particle in the gas filling the chamber. The remaining wires are used to form the electric field of the DC cells so that a proper dependence of the electron drift time on distance from the sensing wire can be obtained. The cells, each constituted by one sensing wire and the surrounding field wires, are arranged in 58 concentric layers in the chamber. Due to a usually higher track density

in KLOE close to the interaction point, the 12 inner cells are sized 2×2 cm while the remaining 46 are larger (3×3 cm) as shown in Figure 3.3 (left).

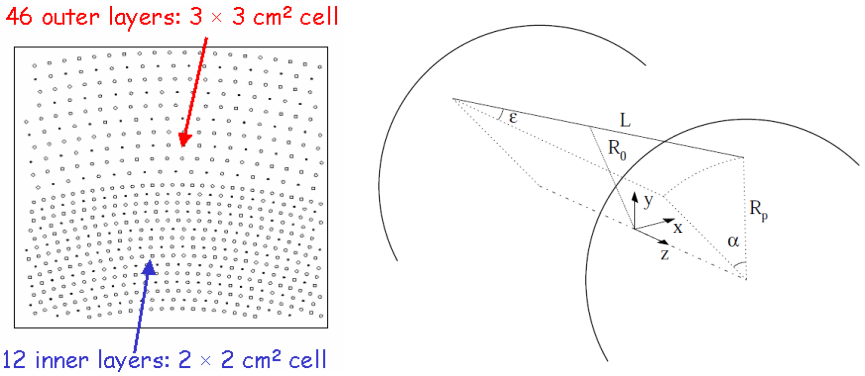

FIGURE 3.3: Alignment of the drift chamber cells (left) and geometry of the wires with respect to the z axis (right). A non-zero stereo angle ε between a wire of length L and the z axis is obtained with a twist of the wire endpoint by an angle α chosen so that the difference of R_0 and R_p distances remains constant independently of the absolute radius. The figures are adapted from [28] and [24], respectively.

Rather than being parallel to the z axis the wires form a small stereo angle ε with the axial direction (Figure 3.3, right). The value of this angle depends on the radius and varies between 60 and 150 mrad while its sign is opposite for neighboring layers. Such geometry allows for the determination of the z coordinate of a DC hit.

The construction materials as well as the gas mixture used in the KLOE DC were carefully chosen with a view to minimizing the probability of kaon regeneration in the chamber. Therefore the walls are built of a low-density and low-Z carbon fiber composite [24]. The gas used is a mixture of helium (90%) and isobutane (10%) due to its minimal density even though it has a higher diffusion of drifting ionization than certain other gases.

The hits recorded by wires and the measured drift times are used to reconstruct the track of the particle. A pion from a $K_S \to \pi^+\pi^-$ decay yields on average about 60 hits in the DC [24]. Moreover, charge collected by the wires provides a measure of the energy deposition which is characteristic of the particle type and thus gives the possibility of particle identification. Finally, the curvature of the reconstructed track resulting from the presence of magnetic field allows for determination of the particle momentum with an excellent relative accuracy of $\frac{\sigma(p)}{p} = 0.4\%$ [27]. The spatial resolution of the drift chamber is less than 200 μm in the transverse plane and about 2 mm in the z coordinate. Decay vertices are reconstructed with an accuracy of about 1 mm [29].

3.2.3 Electromagnetic calorimeter

The purpose of the KLOE electromagnetic calorimeter (EMC) is to record hits of neutral particles and provide Time-of-Flight (TOF) measurement possibility for charged ones.

Hits of gamma quanta in the calorimeter are used to reconstruct the vertices in which only neutral particles are produced such as $K_L \to \pi^0\pi^0$. Therefore the EMC was designed to achieve an excellent time resolution and high detection efficiency for photons in the 20–500 MeV energy range [24].

The technology of a lead-scintillating fiber sampling calorimeter was applied in the KLOE EMC. It is built of a composite of scintillating fibers as an active material and passive lead layers which enhance the electromagnetic shower production. The diameter of fibers is 1 mm whereas the lead layers are 0.5 mm thick and grooved so that the adjacent fibers fill the grooves minimizing the amount of empty spaces. Alternating layers of lead and fibers are glued together with a special epoxy and constitute a bulk material of which the calorimeter modules are built. The lead:fiber:epoxy volume ratio of this composite is 42:48:10 resulting in a density of 5 g/cm^3 and the radiation length X_0 of about 1.5 cm [30].

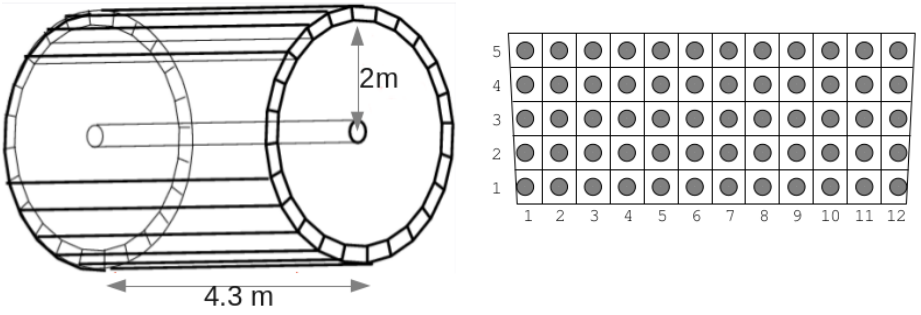

FIGURE 3.4: Modular composition and dimensions of the barrel EMC part (left) and the cell structure of a single module (right). Dark dots represent photomultiplier tubes. The figures are adapted from [31] and [32], respectively.

The EMC structure consists of a central barrel-shaped part and two endcaps closing the barrel on both sides (Figure 3.2). The barrel is built of 24 modules forming a cylinder as shown in Figure 3.4, left. Each module is a uniform piece of the composite described above with about 200 lead-fiber layers perpendicular to the cylinder radius and the fibers lying along the beam axis. The barrel modules are 4.3 m long with a trapezoidal cross section with bases of 52 and 59 cm. Their thickness of 23 cm corresponds to about 15 radiation lengths.

Each of the endcaps is composed of 32 modules, rectangular in cross-section and bent around the pole pieces of the magnet yoke into a C-shape (Figure 3.2). Such a geometry allows to avoid the dead zones between barrel edges and the endcaps resulting in a good coverage of the full solid angle (98% of 4π) by the whole calorimeter. Moreover, the photomultiplier tubes (PMTs) placed at the ends of modules are thus always directed along the magnetic field [30].

Readout of the calorimeter modules is performed by arrays of photomultiplier tubes mounted through light guides at both ends of each module. The guides are divided into blocks of almost square cross section, one for each photomultiplier. This accounts for the division of a whole EMC module into 5 planes and 12 columns of readout segments called cells where each cell is read out by one PMT at each of its ends. The cell structure of a module is shown in the right panel of Figure 3.4.

Such a segmentation allows for determination of the position of particle hit in two dimensions: x-y in the barrel and x-z in the endcaps. When a particle causes an electromagnetic shower in the EMC, its energy is deposited in multiple cells. All cells in which a signal was detected are then analyzed and grouped into clusters [32]. The energy deposited by a particle in the calorimeter is reconstructed as the sum of energies measured in all cells in a cluster with appropriate corrections taken for light attenuation in the scintillating fibers and the efficiency of photomultipliers.

The exact position of a hit in plane perpendicular to the fibers is taken as the energy-weighted average of positions of cluster cells. This method results in a position resolution of ∼1.3 cm in the x and y coordinates [24].

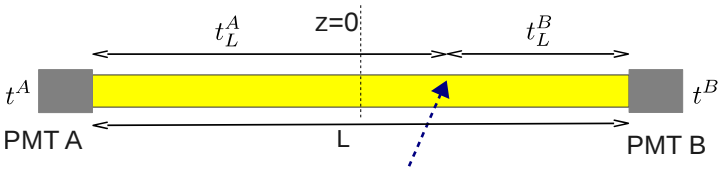

FIGURE 3.5: Times $t^{A,B}$ of light recorded by the two PMT on the ends of a calorimeter cell of length L. Blue dashed arrow indicates a particle hit position and $t_L^{A,B}$ are times of light travelling in the scintillator from this point to PMT A and B.

In order to measure the hit time and position along the cell, the times t^A and t^B of impulses recorded by PMT on both ends A, B of a cell respectively, are considered and used to compare the times $t_L^{A,B}$ of light travelling from the hit point to the two ends of a cell (Figure 3.5). The recorded times $t^{A,B}$ are the sum of light travel times $t_L^{A,B}$ and the time t_{tof} elapsed between the beginning of event and hit in the EMC (for simplicity the cable delays are omitted):

$$t^{A,B} = t_L^{A,B} + t_{tof}. \tag{3.1}$$

The time of a hit for a certain cell is then calculated as an average of t_{tof} obtained from t^A and t^B:

$$t^{cell} = \frac{t^A + t^B}{2} - \frac{L}{2v}, \tag{3.2}$$

where v is the velocity of light in the scintillator and the relation $t_L^A v + t_L^B v = L$ is used. An energy-weighted average of these times for each cell in a cluster is eventually taken as the cluster time T_{cl}.

The z coordinate of the hit in a cell is obtained from the difference of light travel times in the scintillator to cell ends A and B:

$$z^{cell} = \frac{t_L^B - t_L^A}{2} \upsilon, \tag{3.3}$$

The z position is thus determined with respect to the center of a cell as shown in Figure 3.5. Similarly as in case of time, the z coordinate of a whole cluster is the energy-weighted average of z^{cell} over the cluster cells.

The way the times t^A and t^B are measured is related to the KLOE trigger and will be described in Section 3.2.4. Accuracy of time determination depends on the size of the pulse and therefore on the energy deposited in the EMC which results in the resolution of hit time and z position being energy-dependent. Due to this dependence it is justified to take the energy-weighted average of times of all cells in a cluster as the cluster time T_{cl}.

A more detailed description of measurement procedures applied in the KLOE EMC can be found in ref. [30]. Table 3.3 summarizes the resolutions for each of the parameters measured by the KLOE calorimeter.

	resolution
x,y	1.3 cm
z	$\frac{1.2\ cm}{\sqrt{E[GeV]}}$
t	$\frac{54\ ps}{\sqrt{E[GeV]}} \oplus$ 140 ps
E	$\frac{5.7\%E}{\sqrt{E[GeV]}}$

TABLE 3.3: Summary of the KLOE electromagnetic calorimeter resolution.

3.2.4 Trigger

The trigger system applied in KLOE comprises two levels and operates in continuous mode due to high bunch crossing rate of DAΦNE. Level 1 trigger is based on the appearance of isolated energy deposits in the EMC and multiplicity of hits in the DC [27]. This trigger signal is obtained with a small delay and initializes the conversion in the front-end electronics modules. The more detailed information collected from the DC and calorimeter after the arrival of the first level trigger is then processed to obtain the level 2 trigger which validates the first one and starts the readout of data [27].

The Time-to-Digital Converters (TDCs) which measure the times $t^{A,B}$ of light signal arrival to the ends of calorimeter cells are started by the level 1 trigger synchronized with the DAΦNE clock [33]. In consequence, the recorded cluster time T_{cl} is related to the actual

time of flight T_{tof} of a particle from the interaction point to the calorimeter as below:

$$T_{cl} = T_{tof} + \delta_c + N_{bc} \cdot T_{rf}, \tag{3.4}$$

where δ_c accounts for the electronics-related delays, N_{bc} is the number of bunch crossings necessary to generate the trigger and $T_{rf} \approx 2.71$ ns is the period related to DAΦNE radio frequency. The values of δ_c and N_{bc} are determined for each data-taking run using $e^+e^- \to \gamma\gamma$ events. Such approach is caused by the fact that at KLOE high event rate and relatively large spread of particle arrival times make it impossible to identify the bunch crossing which corresponds to a certain event [33]. It also requires the synchronization of level 1 trigger with DAΦNE RF clock which introduces a time jitter resulting in a constant term of 140 ps which has to be added in quadrature to the temporal resolution as shown in Table 3.3.

Chapter 4

The $\phi \to \mathrm{K_S K_L} \to (\mathrm{K_S K_S} \to)\pi^+\pi^-\pi^0\pi^0$ process at KLOE

In the $\phi \to \mathrm{K_S K_L} \to (\mathrm{K_S K_S} \to)\pi^+\pi^-\pi^0\pi^0$ process the $\pi^+\pi^-$ are the only two particles whose tracks are recorded by the drift chamber. As all other participants are neutral, the possibility to reconstruct a kaon decay vertex where only neutral particles are involved is especially important in this case.

Determination of such a neutral decay vertex is a challenging task since typically the vertex resolution for charged decays is better than in case of fully neutral ones. While the $\mathrm{K_{S,L}} \to \pi^+\pi^-$ decay vertex can be found with an excellent accuracy (about 3 mm) using the charged pion tracks measured by the drift chamber, in the $\mathrm{K_{S,L}} \to \pi^0\pi^0$ process no tracks are recorded and the hits of four photons in the electromagnetic calorimeter are the only trace of this event. A great advantage of KLOE, however, is the possibility of kaon four-momentum reconstruction based on the information calculated from the other kaon produced in a two-body ϕ decay. Although it allows for a significant improvement in the accuracy of neutral vertex determination, its usage may lead to a loss of sensitivity to the appearance of kaon regeneration process.

The following chapter starts with a depiction of $\phi \to \mathrm{K_S K_L} \to \pi^+\pi^-\pi^0\pi^0$ process as it appears in KLOE, followed by a short discussion of possibilities of neutral kaon regeneration on elements of the setup. Finally, the method of using EMC clusters and the tagged kaon momentum for reconstruction of a neutral vertex, which is commonly applied at KLOE both to the $\mathrm{K_L} \to \pi^0\pi^0$ and $\mathrm{K_L} \to \pi^0\pi^0\pi^0$ decays, is presented. As this method does not assume the possibility of incoherent kaon regeneration, its performance of reconstruction for events with regeneration is also discussed.

4.1 Properties of the process

Neutral kaons produced in the ϕ meson decay at KLOE move with a relatively small velocity ($\beta \approx 0.22$) which — given their life times as in Table 2.2 — results in a mean path travelled of about 6 mm for K_S and 340 cm for K_L. While directions of their momenta are exactly opposite in the CM reference frame, the small x momentum component of the decaying ϕ needs to be included when transforming the kaons momenta to the laboratory frame.

Figure 4.1 shows a schematic picture of the two possible variants of the process described here, with either $K_S \to \pi^+\pi^-$ and $K_L \to \pi^0\pi^0 \to 4\gamma$ (left) or *vice versa* (right). As one of the kaons decays into a pair of charged pions and the other one into a neutral π pair, only the former of these decays is recorded by the drift chamber. The tracks of charged pions are used to reconstruct the momentum of the decaying kaon with a high accuracy (see Section 3.2.2). The neutral pions produced in the other process, $K \to \pi^0\pi^0$, decay into pairs of γ photons almost in all cases (BR($\pi^0 \to \gamma\gamma$)=(98.823±0.034)% [5]). Due to their short life time (τ_{π^0}=(8.52±0.18)×10^{-17}s [5]) their travelled path is negligible and the whole process appears in the experiment as 4 photons originating at the kaon decay point.

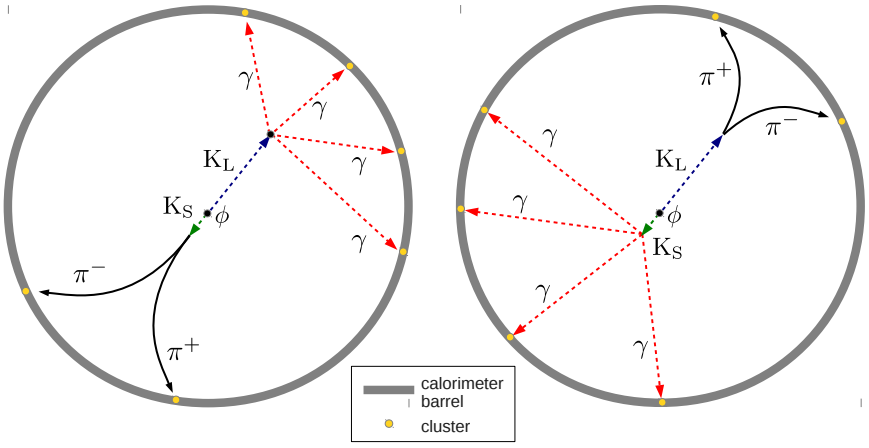

FIGURE 4.1: Schematic view the two possible scenarios of the $\phi \to K_S K_L \to \pi^+\pi^-\pi^0\pi^0$ process in the x-y plane of KLOE. Dashed lines represent particle paths not recorded directly by the detector. For simplicity the paths of π^0 particles are not shown.

The signature of the $\phi \to K_S K_L \to \pi^+\pi^-\pi^0\pi^0$ event at KLOE is therefore:

- two charged tracks connected to one vertex
- at least 4 calorimeter clusters not associated to DC tracks.

Usually there are more than 4 clusters recorded by the EMC in a single event which makes it necessary to choose those which really come from the $K \to \pi^0\pi^0 \to 4\gamma$ decay. To achieve this, all possible pairs of clusters are considered and the two pairs are chosen for whom

the invariant masses of their corresponding $\gamma\gamma$ pairs are closest to the mass of π^0 and for whom the spread of K_L decay points reconstructed separately for each of the 4 clusters is the smallest. The cluster selection procedure must be performed along with the standard vertex reconstruction described in Section 4.3.1.

Since the kaon momentum obtained as a sum of reconstructed momenta of four photons is significantly less accurate than the momentum measured by the drift chamber, in many considerations the precise momentum information of the kaon undergoing the $K \to \pi^+\pi^-$ decay is transformed to the other kaon by taking the opposite in the CM frame and performing a Lorentz transform to the laboratory frame.

4.2 Kaon regeneration at KLOE

The probability of neutral kaon regeneration is significant when the kaon travels through a dense material. Therefore, three solid parts of the KLOE detection setup account for most of the regeneration events.

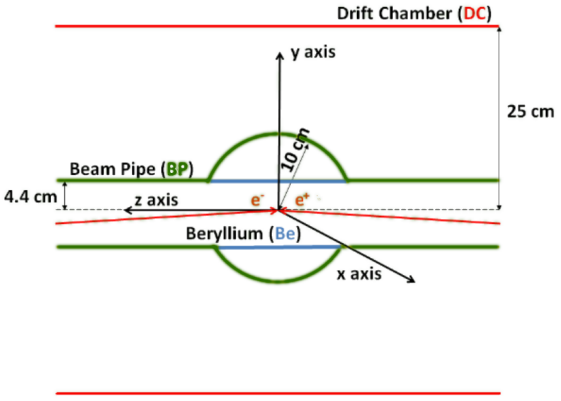

FIGURE 4.2: Location of the three materials closest to the IP which cause kaon regeneration in KLOE: the beryllium cylinder (blue), the beam pipe (green) and the inner wall of the drift chamber (red). The figure is adapted from [8].

Placement of certain regenerating materials is shown in Figure 4.2. The beam pipe (BP) is spherically shaped around the interaction point with a radius of 10 cm in order to ensure vacuum in the volume of about $15\lambda_s$ isotropically around the ϕ decay point and thus minimize the chance of K_S regeneration [24]. The beam pipe is made of a 0.5 mm thick layer of Be-Al alloy. Although regeneration of the short-lived kaon is indeed not observed at KLOE due to its mean life time, K_L is often regenerated when passing through the BP.

In order to ensure continuity of electric field in the spherical part of the BP, a cylinder made of beryllium foil is inserted inside it as shown in Figure 4.2. The radius of the cylinder is 4.4 cm. Despite the foil thickness of 50 μm, it also becomes an important source of K_L regeneration in KLOE. Third of the materials is the cylindrical inner wall

of the drift chamber made of a 750 μm layer of carbon fiber and 150 μm of aluminum [8] with a radius of 25 cm.

A detailed study of regeneration at KLOE can be found in ref. [8]. It is shown there that the probability of coherent regeneration (which does not change the momentum direction of the undergoing kaon) is two orders of magnitude smaller than for incoherent regeneration which makes this process negligible at KLOE. The dominating incoherent regeneration is associated with a change of the kaon direction. Let us define the regeneration angle as an angle between momenta of the original K_L and the K_S produced in regeneration. Distributions of this angle obtained with Monte Carlo-simulated events are shown in the left plot of Figure 4.3. The Monte Carlo simulation can be also used to evaluate the

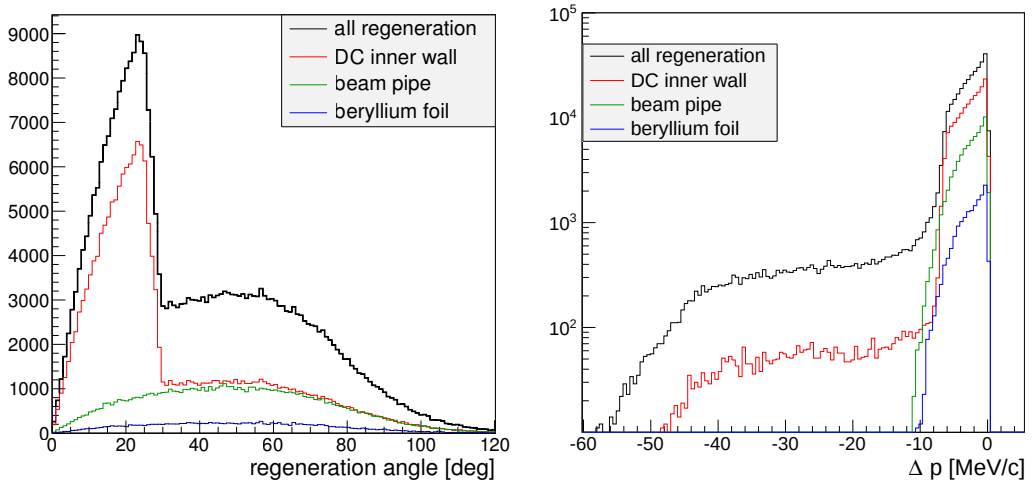

(a) (b)

FIGURE 4.3: Distributions of the regeneration angle (left) and momentum modulus change due to regeneration (right) for all regeneration events (black histogram) and for certain regenerating materials in KLOE (colors correspond to Figure 4.2). The distributions were obtained using Monte Carlo-simulated events.

change of kaon momentum value caused by regeneration. Right plot of Figure 4.3 shows the distribution of the change of kaon momentum modulus defined as $\Delta p = |\vec{p}_{K_S}^{\,regen.}| - |\vec{p}_{K_L}^{\,initial}|$. It is visible that only regeneration on the DC wall may modify the kaon momentum significantly. Taking into account the mean neutral kaon momentum of 127 MeV/c, the maximum momentum change due to regeneration on the beryllium or the beam pipe is about 8%. Such a maximum change in momentum corresponds to an average difference in the regenerated K_S path of about 0.5 mm.

The probabilities of regeneration of a kaon passing a certain material as well as cross sections for these processes were estimated for all main regenerating materials of KLOE. Table 4.1 contains a summary of available measurements of cross section values for regeneration at KLOE.

source	Regeneration cross section [mb]		
	berylium foil	beam pipe	DC inner wall
I. Balwierz (preliminary result) [8]	$50\pm0.7^{stat}\pm5.0^{syst}$	$77.6\pm0.3^{stat}\pm7.8^{syst}$	$75.7\pm0.3^{stat}\pm7.6^{syst}$
S.Bocchetta thesis [34]	—	$59.6\pm0.6^{stat}\pm6.0^{syst}$	$60.2\pm0.8^{stat}\pm6.0^{syst}$
CMD-2 [35]	55.1 ± 7.7	—	—
I. Balwierz (refined analysis)	$54.1\pm2.3^{stat}\pm1.8^{syst}$	$91.7\pm0.9^{stat}\pm8.3^{syst}$	$113\pm1^{stat}\pm11^{syst}$

TABLE 4.1: Cross sections for K_L regeneration on main regenerating materials of the KLOE detector according to several measurements: preliminary results by I. Balwierz [8], previous results by S. Bocchetta [34], measurement at the CMD-2 experiment [35] and recent refined results by I. Balwierz (from private communication).

4.2.1 Influence of regeneration on interferometric studies

In order to perform interferometric measurements with neutral kaon pairs, a distribution of differences of kaon decay times has to be collected and analyzed as described in Section 2.3.2. This distribution is, however, affected by the events where K_L is transformed into K_S in the regeneration process. Since it predominantly occurs at the regenerators located in a well-defined distance from the interaction point and the regenerated K_S decays quickly compared to the original K_L, the regeneration leads to the appearance of three structures of events which are not expected in the ideal distribution shown in Figure 2.1. The location of these structures corresponds to the flight time of K_L before it is regenerated. First excess of events appears at about $7\tau_s$ and is caused by the beryllium foil, the second is at $\sim 17\tau_s$ and corresponds to regeneration on the beam pipe. Finally, regeneration on the drift chamber wall should contribute to the distribution at $\Delta t \approx 45\tau_s$. The latter, however, is the least harmful as it lies away from the most important region ($\Delta t \approx 0$).

Figure 4.4 shows a distribution of decay time differences of the $\phi \to K_S K_L \to \pi^+\pi^-\pi^+\pi^-$ process. A peak caused by regeneration on the beam pipe is clearly visible due to the fact that at the moment of regeneration of K_L into K_S, the original quantum entanglement between a pair of neutral kaons is lost and therefore the decays of the regenerated K_S should not be included in the distribution. The scale of the peak makes it apparent that the influence of events with regeneration can by no means be neglected in the interferometric studies.

Regeneration, especially taking place in beryllium and in the beam pipe, constitutes background for the study of $\phi \to K_S K_L \to \pi^+\pi^-\pi^0\pi^0$ process and requires efficient methods to reject these events. Unfortunately, the standard reconstruction method used for the $K_L \to \pi^0\pi^0$ vertex is not sensitive to the appearance of regeneration in the $K_L \to K_S \to \pi^0\pi^0$ process, as it will be shown in the next section.

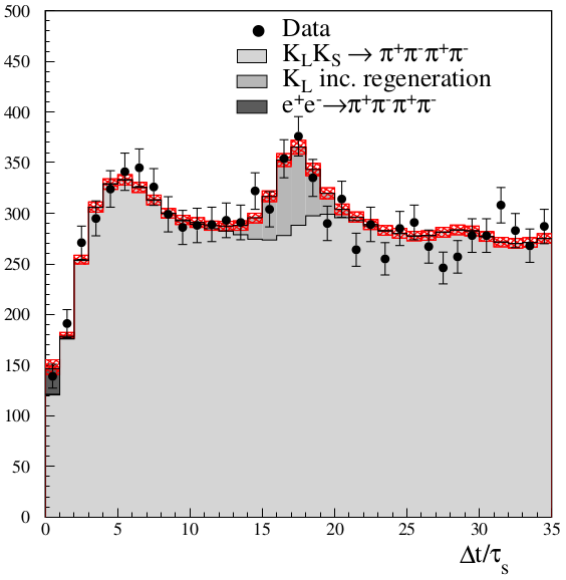

FIGURE 4.4: Fit (solid histogram) of the intensity distribution to data in the analysis of the $\phi \to K_S K_L \to \pi^+\pi^-\pi^+\pi^-$ process. An excess of events at $\sim 17\tau_s$ caused by regeneration on the beam pipe is clearly visible. The figure is adapted from [36].

4.3 Standard $K_L \to \pi^0\pi^0$ reconstruction method

4.3.1 Principle of the reconstruction

In the case of a neutral kaon decaying into neutral pions only, the only information recorded by the detector are the photons produced in pairs in the π^0 decays which hit the electromagnetic calorimeter. Fortunately, if the other of the kaon pair decayed into charged pions, the information on its momentum vector obtained from the DC can be used to estimate the momentum direction of the kaon which decayed through the neutral channel. It is then enough to search for the decay point along the kaon momentum direction which corresponds to the path of its flight.

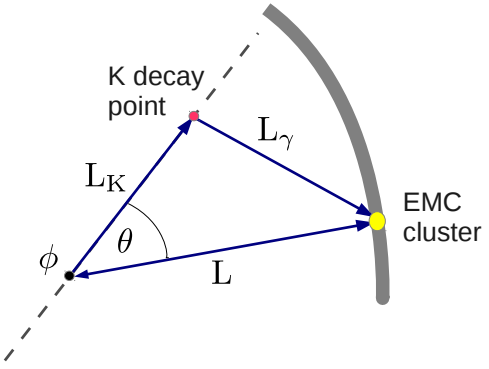

FIGURE 4.5: The *time-of-flight triangle* used to determine the kaon decay point. Dashed grey line denotes the kaon momentum direction tagged with the other kaon.

The determination of the decay point on this path then requires only one calorimeter cluster and is in fact done independently for each of the clusters registered in an event. The centroid of the cluster, the interaction point where the kaon is created and its decay point form a *time-of-flight triangle*, schematically shown in Figure 4.5. Two edges of this triangle are the flight paths of the kaon (of the length L_K) and of the γ quantum (of the length L_γ). Length of the third edge L can be easily calculated using the interaction point location and the EMC cluster coordinates. Considering the fact that the cluster time equals to the sum of times of flight of the kaon and photon, leads to equation (4.1). Moreover as the θ angle between the kaon flight direction and the L segment is known, the law of cosines can be written for the time-of-flight triangle as in equation 4.2.

$$t_\gamma = \frac{L_K}{c\beta} + \frac{L_\gamma}{c} \tag{4.1}$$

$$L_\gamma^2 = L^2 + L_K^2 - 2LL_K cos(\theta) \tag{4.2}$$

Solution of the equation system (4.1–4.2) yields the length L_K of the kaon flight path, which in turn determines two possible points of K decay along its flight direction, one of which is easily discarded [37].

This method is used to find the kaon decay point independently using each of the neutral clusters recorded in the event. As it is not known *a priori* which of the clusters come from the $\pi^0\pi^0 \to 4\gamma$ decay, the reconstructed vertices are used to calculate invariant masses of all possible $\gamma\gamma$ pairs. The two pairs are chosen based on two criteria — their invariant masses should be close to π^0 mass and the K_L decay points obtained using each of the four clusters should have the smallest spread along the kaon momentum direction.

Once the 4 clusters are chosen, an energy-weighted average of the L_K values obtained for each of them is eventually taken as the neutral vertex position. Using the energies of clusters as weights is justified by the fact that the resolution of the kaon path length determination with this method depends on the cluster energy as $\sim 1/\sqrt{E}$ [37].

4.3.2 Resolution of the method

Resolution of the vertex reconstruction can be tested using experimental data by studying the $K_L \to \pi^0\pi^+\pi^-$ [33] decays. The vertex obtained with photons from the π^0 decay is compared to the one found with the charged pion tracks. Results of such a resolution analysis are shown in Figure 4.6. A decrease of the L_K accuracy with distance from the interaction point is caused by the finite angular accuracy of the tagged kaon momentum direction. It should be noted, however, that the resolution for the $K_L \to \pi^0\pi^0$ process is better because of a higher number of clusters entering the average [30].

Resolution of this method for the $K \to \pi^0\pi^0$ decay vertex position was studied using reconstructed events from Monte Carlo (MC) simulation. Figure 4.7 left shows the distribution

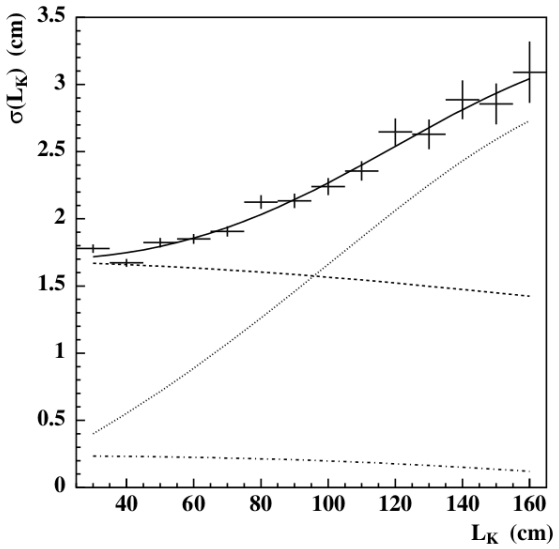

FIGURE 4.6: Resolution of the L_K kaon decay length determination by the standard algorithm as a function of L_K. Main contributions to the uncertainty come from the calorimeter cluster position uncertainty (dot-dashed line), the cluster time (dashed line) and the K_L flight direction (dotted line). The figure is adapted from [33].

of differences between the x coordinate of MC-generated and reconstructed kaon decay vertex position as a function of vertex distance from the ϕ decay point. Similar distributions for each of the vertex coordinates may be used to estimate the spatial resolution of reconstruction with the mean spread of these differences in vertical slices of the distribution. Right-side of Figure 4.7 presents the resolution obtained this way. Horizontal bars indicate width of the slices whereas vertical bars correspond to standard deviation of the estimated resolution.

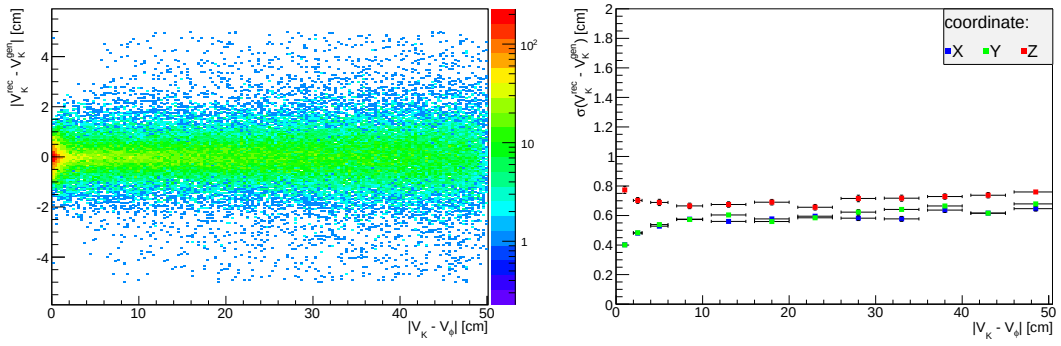

FIGURE 4.7: Left: distribution of differences in the x coordinate of reconstructed (V_K^{rec}) and MC-generated(V_K^{gen}) kaon vertices as a function of distance from the ϕ meson (V_ϕ) to kaon (V_K) decay vertex. Right: spatial vertex resolution in each coordinate as a function of the distance between decay vertices of kaon (V_K) and ϕ meson (V_ϕ). The points indicate distribution widths in vertical slices of the left-side plot in case of x and similar distributions in case of y and z coordinates. Horizontal error bars correspond to the width of each slice.

4.3.3 Performance for events with regeneration

The reconstruction method described above assumes that the decay vertex of the kaon lies along its initial flight path. Figure 4.8 schematically shows the process $\phi \to K_L K_S \to K_S K_S \to \pi^+\pi^-\pi^0\pi^0$ where the long-lived kaon is regenerated with a change in its momentum direction. The created K_S then travels a short distance moving away from the original kaon path. The standard reconstruction, however, always determines the decay vertex along this direction. As a result, the reconstructed vertex does not correspond to the real point where the regenerated kaon decayed into pions. Although the discrepancy is small due to the short life time of K_S, the fact that the resulting reconstructed event resembles a good signal event is an important obstacle to regeneration background rejection.

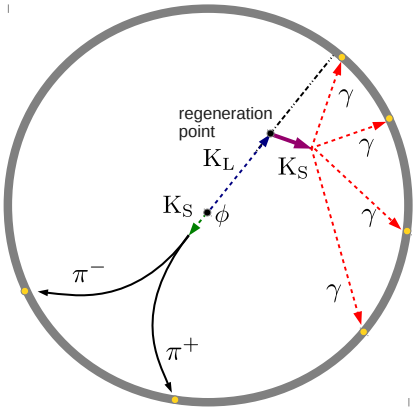

FIGURE 4.8: Schematic view of an event with K_L regeneration. The dotted-dashed line represents the momentum direction of K_L obtained from the decay of K_S. Even though the regenerated kaon decays away from this line, the vertex is still sought only along this direction.

In order to recognize the regeneration taking place in an event, an auxiliary vertex reconstruction method for $K_L \to \pi^0\pi^0$ is necessary, i.e. one which does not assume the vertex location along the initial kaon momentum direction. Such a reconstruction algorithm is proposed and described in the next chapter.

Chapter 5

New reconstruction method

The standard reconstruction method of the $K_L \to \pi^0\pi^0$ vertex used in analysis of the $\phi \to K_S K_L \to \pi^+\pi^-\pi^0\pi^0$ process takes a great advantage of presence of a tagging kaon which decays into charged pions. Its momentum gives a very accurate information on the direction of flight of the kaon which undergoes a decay into $\pi^0\pi^0$. This information is used along with the spatial and temporal coordinates of the clusters recorded by the calorimeter to determine the neutral decay vertex. Although the EMC of KLOE is characterized by an excellent resolution, its measurements cannot exceed the precision of a drift chamber. The kaon momentum direction is then the most accurate of the values used in the vertex reconstruction. Unfortunately, the assumption that the kaon decay vertex lies along this direction is only valid if the kaon was not regenerated as it was shown in the previous chapter. Therefore in order to account for the possibility of regeneration, an alternative method of $K_L \to \pi^0\pi^0$ vertex reconstruction is needed which does not assume the vertex lying along the path of the original kaon. Then, however, the tagged momentum direction cannot be explicitly used. Instead, a modulus of this momentum is utilized and the reconstruction is based exclusively on the calorimeter clusters created by γ hits. Such a reconstruction algorithm was invented and proposed as an auxiliary method. Details of this algorithm are presented in the following chapter.

5.1 Requirements

In the $K_L \to K_S \to \pi^0\pi^0$ process the momentum direction of incoherently regenerated K_S is usually different from the one of the original K_L (see Figure 4.3, left). Therefore, in case of regeneration, in order to properly reconstruct a $K_L \to \pi^0\pi^0$ vertex, the method described here cannot depend on the momentum vector of the tagging kaon. This, however, implies that in case of $K_S K_L \to \pi^+\pi^-\pi^0\pi^0$ events part of experimentally available information is not used.

It should then be emphasized that the new reconstruction method does not aim at achieving a higher resolution than the standard one. Rather than that it should provide an accuracy sufficient to distinguish events with regeneration ($K_S K_L \to K_S K_S \to \pi^+\pi^-\pi^0\pi^0$) from good $K_S K_L \to \pi^+\pi^-\pi^0\pi^0$ events, for which purpose it is exclusively targeted.

5.2 Working principle

The information on a $K_{S,L} \to \pi^0\pi^0 \to 4\gamma$ event available from the detector which may be used for the vertex reconstruction consists of spatial and temporal coordinates of four neutral clusters in the electromagnetic calorimeter (associated with the four photons). The temporal coordinate of a cluster, i.e. the time of its recording is related to the time T_{tof} elapsed between the ϕ decay and the γ hit into the EMC as in eq. (3.4). For simplicity, in further considerations T_{tof} will be referred to as the cluster time. The spatial and temporal coordinates of the i-th cluster will be denoted with capital letters: X_i, Y_i, Z_i, T_i. The four clusters to be used are chosen prior to reconstruction using the procedure described in Section 4.3.1.

Let us now assume that the long-lived kaon produced in a ϕ decay has lived for time t before decaying into $\pi^0\pi^0$ in a point (x, y, z). Due to short lifetime of neutral pions the photons from their decays are created approximately in the same point. The cluster time for each of the clusters created by photons is therefore equal to a sum of flight times of K_L and the respective photon:

$$T_i = t + t_{\gamma i}, \qquad i = 1, \ldots, 4. \tag{5.1}$$

Although the times t_γ vary between the EMC clusters, all photons must have been created in the same point being also the kaon decay vertex. Thus the problem of localizing the vertex is identical with finding a common origin point of the four photons. This situation is schematically presented in Figure 5.1.

For a given time of flight of a gamma (t_γ) and the point where it hit the EMC, a set of its possible origin points is represented by a sphere centered at the cluster spatial position and of the radius corresponding to path travelled by a photon in time t_γ:

$$S^i((X_i, Y_i, Z_i), ct_{\gamma i}), \qquad i = 1, \ldots, 4, \tag{5.2}$$

where c is the velocity of light. If the γ times of flight are eliminated using eq. (5.1), full equations representing the aforementioned spheres for each of the photons are of the following form:

$$(X_i - x)^2 + (Y_i - y)^2 + (Z_i - z)^2 = (T_i - t)^2 c^2, \qquad i = 1, \ldots, 4, \tag{5.3}$$

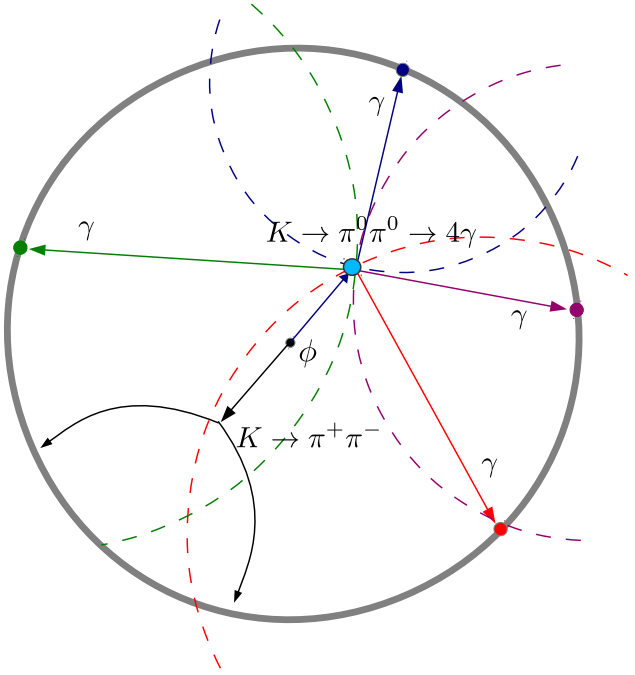

FIGURE 5.1: Idea of the $K \to \pi^0\pi^0$ decay vertex reconstruction. For simplicity the event is shown in a 2-dimensional transverse section of the detector. Dashed arches represent sets of possible origin points of photons which created clusters in the EMC (gray ring). Blue dot denotes the intersection of these sets which corresponds to the $K \to \pi^0\pi^0$ vertex.

where x, y, z and t are not known[1]. The above constitutes a system of 4 equations with 4 unknowns which can be solved to obtain the intersection point (x, y, z) of the spheres from eq. (5.2) as well as the kaon flight time t.

Although the problem of solving this system of equations is to some extent similar to finding a geometrical intersection of spheres, it should be noted that the radii of spheres in this case are not constant. Instead, they are parametrized by an additional variable t which adds a substantial complication to the problem.

Finally, it is worth stressing that this reconstruction algorithm strongly relies on a proper choice of the four calorimeter clusters associated with the $K_L \to \pi^0\pi^0 \to 4\gamma$ decay. This is because information on all of the clusters enters the reconstruction simultaneously in contrast with the standard method described in Section 4.3.1. Therefore wrong choice of even one of the clusters might significantly affect the result of reconstruction.

5.3 Implementation of the method

A complete analytical solution to the above system was found and its detailed description is provided in Appendix A. This solution comprising the spatial coordinates of the vertex

[1] As the general form of equation describing a sphere of radius R centered at (x_c, y_c, z_c) is $(x_c - x)^2 + (y_c - y)^2 + (z_c - z)^2 = R^2$.

(x, y, z) and the time of kaon flight t is determined with a two-fold ambiguity which results from the time being a solution of the quadratic equation (A.15). In further considerations the two solutions (see equations (A.17–A.18) in Appendix A) will be referred to as solution 1:

$$(t_1, x(t_1), y(t_1), z(t_1)), \quad t_1 = \frac{-q - \sqrt{q^2 - 4pr}}{2p}, \tag{5.4}$$

and solution 2:

$$(t_2, x(t_2), y(t_2), z(t_2)), \quad t_2 = \frac{-q + \sqrt{q^2 - 4pr}}{2p}, \tag{5.5}$$

where the coefficients p, q and r are defined in the aforementioned Appendix A.

The ambiguity of solutions may appear in two possible ways:

1. One of the two solutions corresponds to a real kaon decay vertex whereas the other one is a mathematical artifact and has to be rejected.
2. Both solutions differ to a small extent only resulting from the numerical inaccuracies in their determination. This case corresponds to an ideal situation of $q^2 - 4pr \approx 0$ in eq. (A.17) where the single existing solution was split due to the fact that the solutions are evaluated with finite precision.

It is crucial both that the these two cases are distinguished and that in the first case a proper solution is selected rather than the artifact one. In order to ensure this, several criteria were devised to be applied to pairs of solutions obtained for each event. These criteria are based on physical constraints a real decay vertex must satisfy:

1. $t \geq 0$ and $t < 60$ ns as the time of kaon flight in the detector must be positive and not exceed the time of a particle with $\beta_K \approx 0.22$ travelling the maximal possible distance in the detector (which is about 262 cm along a diagonal from the e^+e^- collision point to the edge of EMC barrel).
2. The spatial vertex coordinates must lie in the geometrical limits of the detector. The detector volume is a cylinder constrained in transverse radius by $r_T = \sqrt{x^2 + y^2} <$ 200 cm and in the z coordinate by $|z| < 169$ cm.
3. The kaon originating at the IP with its velocity must have been able to reach its decay point (x, y, z) within its flight time t.

The third criterion is the strongest and requires a broader explanation. If the kaon vertex spatial location is denoted by $\mathrm{V_K} = (x, y, z)$ and the ϕ decay point (interaction point) by V_ϕ then the length of path travelled by a kaon before its decay can be calculated as[2]:

$$\mathrm{S} = |\mathrm{V_k} - \mathrm{V}_\phi|. \tag{5.6}$$

If the i-th solution for the vertex $(\mathrm{V_{Ki}}, t_i)$ is physical, the condition must hold:

$$\upsilon\, t_i - \mathrm{S_i} = 0, \tag{5.7}$$

[2]So far let us assume no regeneration in the event.

where v is the kaon velocity. Even though the direction of K_L momentum vector calculated using the tagging kaon is not reliable in this method, its bare modulus can be safely used to determine the kaon velocity v.

If one of the two solutions is rejected by any of the aforementioned criteria, the remaining one is chosen as the location of reconstructed kaon decay vertex. Otherwise the solutions are checked for being close to each other. If their difference is below a threshold value of 1 ns, an arithmetic average of both solutions is used as the final reconstruction result.

5.4 Method validity studies

The new reconstruction method was tested using a sample of Monte Carlo-simulated (MC) events of the $\phi \to KK \to \pi^+\pi^-\pi^0\pi^0$ process containing both signal and regeneration. Since the simulated events are generated artificially, in their case all parameters of the process are known exactly. Events described using these exact values will be referred to as generated events. For each generated event a detector response is determined and then cluster coordinates are reconstructed in the same way as it is done for the experimental data. If the events are described by such reconstructed parameters, they will be called reconstructed events.

5.4.1 Spatial resolution of the method for generated events

MC generated events were used to test the performance of the reconstruction method in an ideal case. First, the possibility of selecting the proper solution was tested. As mentioned in the previous section, criterion 3 is the most powerful tool to reject non-physical solutions for the vertex. Feasibility of its use can be estimated with the respective distribution of $(v\,t_i - S_i)$ values calculated for first and second solution. Such a plot for reconstruction of generated events is shown in Figure 5.2. Since the difference $(v\,t_i - S_i)$ must be close to zero for a vertex to be physical, it is visible that criterion 3 can be successfully used to select one of the solutions as for all events at least one of the solutions satisfies this condition. If both solutions fulfill it, they must be checked for being in fact one split solution.

For generated MC events, the criteria described in sec. 5.3 allowed for selection of one proper solution in a majority of events as shown in Table 5.1. A worse result in case of regeneration events results from the calculation of kaon path length as in eq. (6.5) which does not assume the kaon flight direction change due to regeneration.

For the events where a single physical solution was distinguished, the spatial resolution of the vertex obtained with the new reconstruction method was analyzed. Figure 5.3 shows the resolution in each coordinate as a function of vertex distance from the IP. The estimated

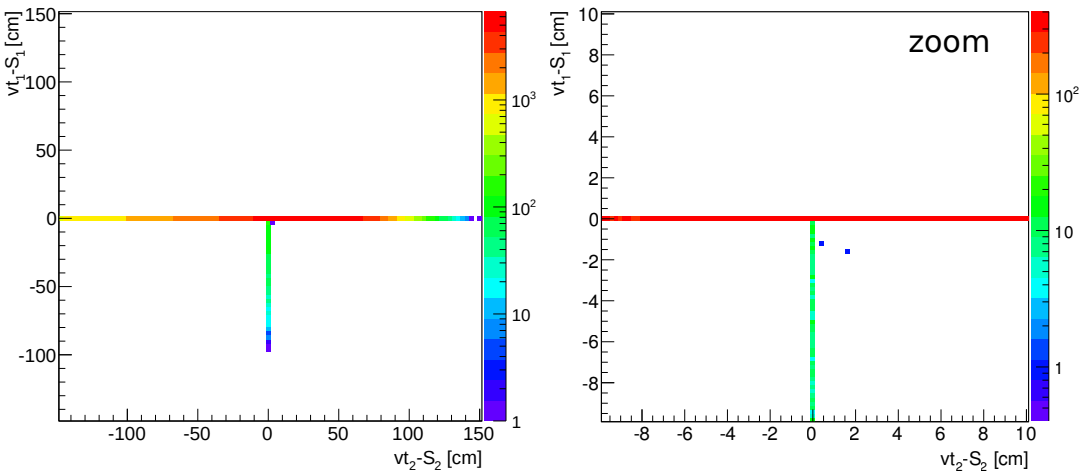

FIGURE 5.2: Left: Two-dimensional distribution of the $v\,t_i - \mathrm{S}_i$ values for solutions 1 and 2 obtained in the vertex reconstruction for generated MC events. Right: magnification of this distribution for the ranges $|v\,t_i - \mathrm{S}_i|$ <10 cm. At least one of the solutions always satisfies the $v\,t_i - \mathrm{S}_i \approx 0$ criterion which allows for good selection of the single solution describing the real vertex.

	signal	regeneration
1. one solution chosen	97.9%	90.8%
2. two solutions	2.0%	1.95%
3. both rejected	0.1%	7.25%

TABLE 5.1: Results of physical solution selection for generated MC events. Signal and regeneration events are analyzed separately. Only in case 1 one solution is chosen unambiguously. In case 2 none of two solutions could be discriminated and in case 3 both solutions were rejected by the criteria.

resolution is of the order of 10^{-5} cm which is below the measurable scales in KLOE and probably results only from numerical inaccuracies appearing in the reconstruction.

This result shows that in an ideal case where exact cluster coordinates are used as input to the reconstruction, the exact position of real vertex is obtained, which proves that the new reconstruction algorithm is correct.

5.4.2 Spatial resolution for reconstructed events

Reconstruction of the neutral vertex was tested with the use of reconstructed MC events which are affected by experimental inaccuracy. Figure 5.4 shows a two-dimensional distribution of the $(v\,t_i - \mathrm{S}_i)$ values for both solutions obtained in the same manner as the plot in Figure 5.2.

The distribution of $(v\,t_i - \mathrm{S}_i)$ differences for reconstructed MC events is substantially broader than for generated MC in case of both solutions. Therefore the third criterion from

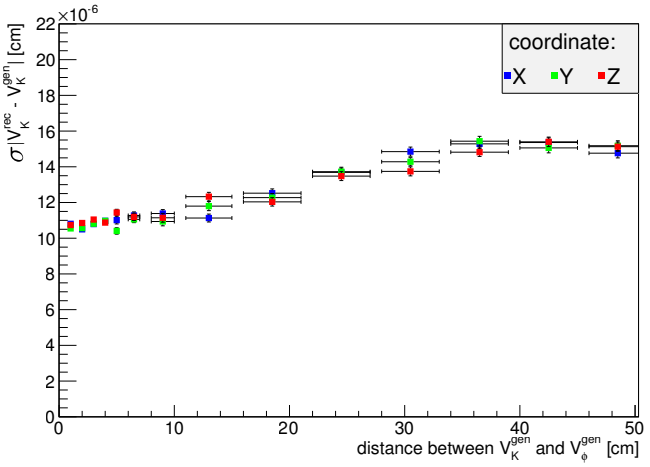

FIGURE 5.3: Spatial vertex resolution in each coordinate as a function of vertex distance from the ϕ decay point obtained for generated MC events. Vertical error bars (too small to be visible) represent the error on determination of width of the distributions of differences (for each coordinate) between reconstructed (V_K^{rec}) and generated (V_K^{gen}) kaon vertices. Horizontal bars correspond to ranges of distance between generated kaon (V_K^{gen}) and ϕ meson (V_ϕ^{gen}) vertices chosen so as to contain the same number of events. This result shows that using exact cluster parameters in the reconstruction leads to a precise vertex location proving validity of the new method.

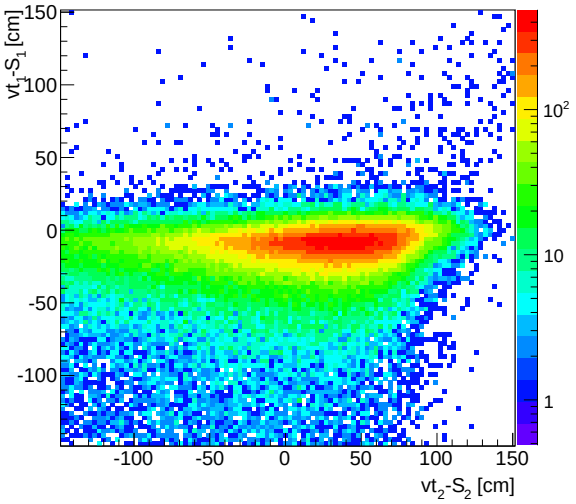

FIGURE 5.4: Two-dimensional distribution of the $v\,t_i - \mathrm{S}_i$ values for solutions 1 and 2 obtained in the vertex reconstruction for reconstructed MC events. The inaccuracy of input parameters in the reconstruction leads to solutions which do not satisfy the $v\,t_i - \mathrm{S}_i \approx 0$ criterion well.

Section 5.3 which is based on at least one of solutions giving the value of aforementioned difference close to zero, could not be applied in this case as it would reject a majority of all events. This, however, leads to a decrease in the capability to select one physical solution as it can be seen in Table 5.2.

In addition to strongly reducing the number of useful events (with one reliable solution for the vertex), the inaccuracy of input parameters also affects the final spatial resolution of

	signal	regeneration
1. one solution chosen	18.9%	17.7%
2. two solutions	29.3%	29.9%
3. both rejected	51.8%	52.4%

TABLE 5.2: Results of physical solution selection for reconstructed MC events. Signal and regeneration events are analyzed separately. Only in case 1 one solution is chosen unambiguously. In case 2 none of two solutions could be discriminated and in case 3 both solutions were rejected by the criteria.

the vertex. The resolution is presented in Figure 5.5 showing a poor result of about 15 cm spread of distances between the generated and reconstructed vertex in each coordinate. An even worse performance is observed for events close to the ϕ decay vertex. This trend is

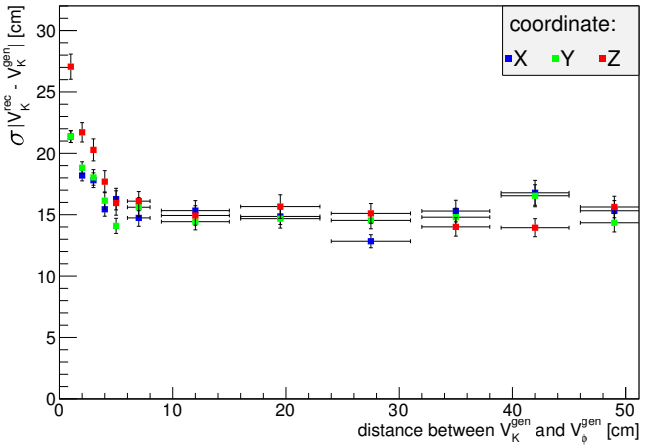

FIGURE 5.5: Spatial vertex resolution in each coordinate as a function of vertex distance from the IP obtained for reconstructed MC events. Inaccuracy of reconstructed cluster coordinates used as input in the vertex reconstruction results in a poor resolution of the vertex location.

caused by the fact that in case of $K_{S,L} \to \pi^0\pi^0 \to 4\gamma$ decay close to the detector center, the spheres of possible gamma origin points for all clusters are almost of the same radii whereas for peripheral decays the sphere radii may vary strongly. Figure 5.6 schematically shows both cases (using two spheres for simplicity) where experimental errors of cluster times cause a smearing of the spheres' surfaces (denoted with colored bands). The uncertainty of the spheres' intersection point is bigger when all the radii are large (which is the case for decays close to detector center), as it can be seen on the left side of Figure 5.6 which leads to a worse resolution of decay vertices close to the ϕ decay point.

The above results indicate that the accuracy with which the cluster coordinates are determined experimentally is not sufficient to reconstruct the $K_{S,L} \to \pi^0\pi^0$ decay vertex with a satisfactory spatial resolution using the presented method. However, the accuracy of input data used in the reconstruction can be noticeably improved in order to achieve a better vertex resolution with the help of additional physical constraints. This fit will be presented in the next chapter.

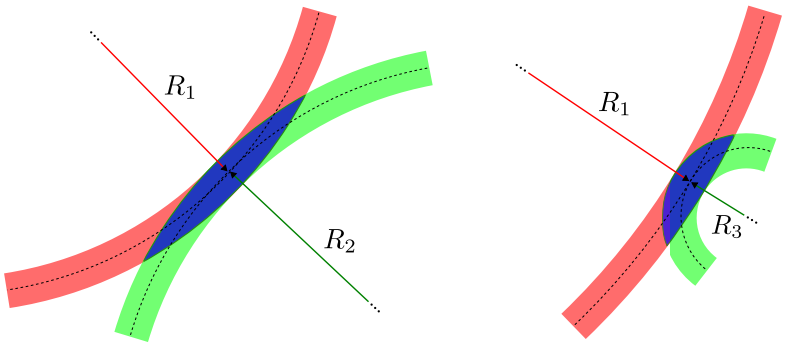

FIGURE 5.6: Intersections of two spheres (dashed lines) with experimental inaccuracy (colored bands). Left picture shows the case of spheres with similar radii $R_1 \approx R_2$ while on the right picture one sphere is significantly larger: $R_1 \gg R_3$. Blue region represents the area where the intersection point may be found and its size corresponds to the uncertainty of vertex location.

5.4.3 Influence of input data inaccuracy on spatial resolution

Uncertainty of the vertex reconstruction depends on the resolution of the position and of the time reconstruction of the EMC clusters. In this section influence of the reconstruction resolution of each cluster coordinate on the accuracy of vertex reconstruction is investigated. For this purpose the vertex is reconstructed using the simulated samples of events for which only one coordinate was smeared according to the gaussian distribution and the other coordinates were not smeared. Resolution of vertex location obtained in these cases as a function of the distance from the interaction point is shown in Figure 5.7.

It is visible that the uncertainty of EMC cluster times gives a significantly larger contribution to the vertex inaccuracy than errors on spatial coordinates of clusters. When the latter are considered, the inaccuracies of vertex reconstruction due to the uncertainty of X and Y are similar and smaller than due to the smearing of Z coordinate, as it was expected due to worse EMC resolution in the Z direction (see Table 3.3). A conclusion can be drawn that the vertex location resolution is dominated by the experimental error in determination of cluster times.

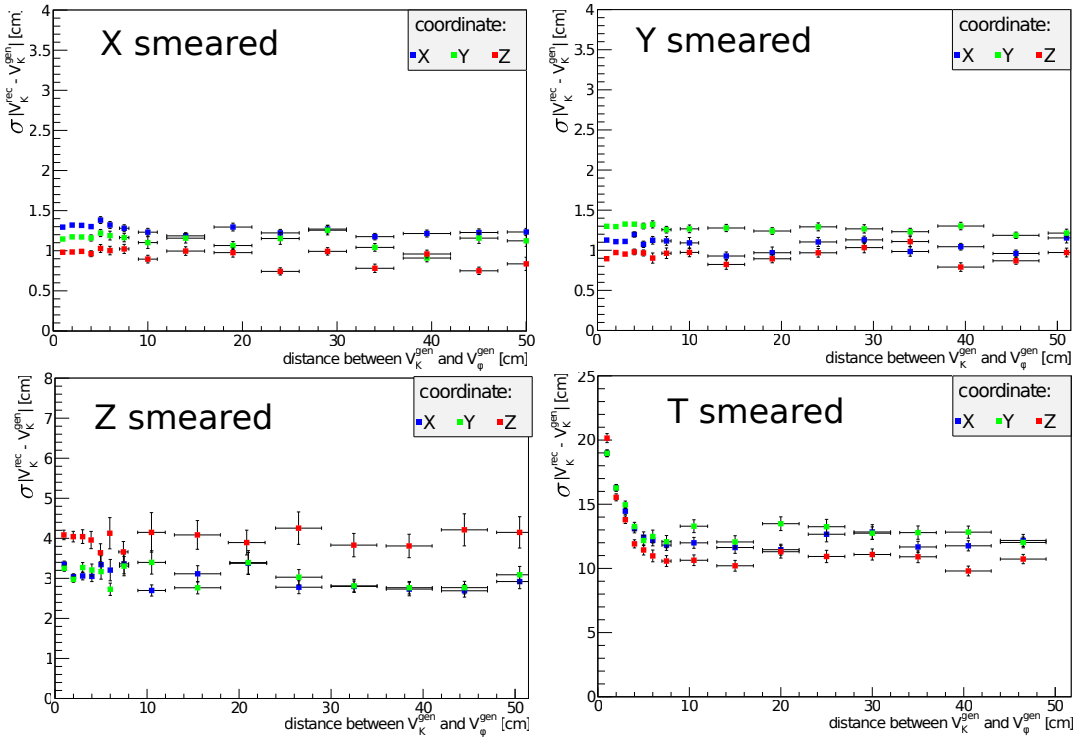

FIGURE 5.7: Resolution of vertex reconstruction when one of the input cluster coordinates is smeared with an experimental uncertainty while other parameters are exact (MC-generated). The upper plots correspond to smeared cluster X (left) and Y (right) coordinates, lower left plot corresponds to smeared Z cluster coordinates and lower right plot — to smeared cluster times.

Chapter 6

Tuning the input parameters

Tests of the new $K \to \pi^0\pi^0$ vertex reconstruction method with Monte Carlo-generated events described in the previous chapter have shown that the principle of its operation is correct as it yields a precise vertex location using ideally accurate input data. On the other hand, it was also discovered that when the reconstructed cluster coordinates with an experimental uncertainty are used, the inaccuracy of these data strongly affects the reconstructed vertex location resulting in a poor spatial resolution.

Since precision of the cluster coordinate reconstruction is limited by finite resolution of KLOE calorimeter (see Table 3.3), additional information needs to be introduced to the system in order to improve the accuracy of vertex reconstruction. This can be achieved by imposing several constraints on the properties of the considered system based on physical conditions which must be satisfied by each event of the process of interest.

Two major constraints were found for the case of $K \to \pi^0\pi^0 \to 4\gamma$ decay which include information not exploited in the bare reconstruction of the respective vertex. The way to include these constraints in the considered problem follows a general scheme of a kinematic fit. The following chapter gives a detailed description of the procedure of this fit and influence of its application on the vertex reconstruction.

6.1 Fitting procedure

6.1.1 Principle of the fit

The principle of a kinematic fit relies on an assumption that experimentally measured quantities are randomly distributed around the respective exact values with a normal distribution whose width corresponds to their measurement uncertainty. In such a case a variation of these values in ranges allowed by their uncertainty so that they satisfy additional physical constraints to a higher extent should result in these quantities being shifted

towards their exact values and thus increasing their accuracy. This requires formulation of the penalty functions as functions of the vector $\mathbf{x} = (x_i)_{i=1,\ldots,n}$ of n parameters being tuned. The penalty functions (constraints) $\mathrm{C}(\mathbf{x})$ are chosen so that constraints take the form:

$$\mathrm{C}(\mathbf{x}^{true}) = 0, \tag{6.1}$$

where $\mathbf{x}^{true}$ is a vector of exact values corresponding to the measured parameters[1]. In order to control the degree of parameter variation from reconstructed values $\mathbf{x}^{rec}$, the following function of varied parameters $\mathbf{x}^{var}$ is also introduced:

$$\mathrm{F}(\mathbf{x}^{var}) = \chi^2(\mathbf{x}^{var}) + \sum_j \mathrm{C_j^2}(\mathbf{x}^{var}), \tag{6.2}$$

where j iterates over all constraints and:

$$\chi^2(\mathbf{x}^{var}) = \sum_{i=1}^{n} \left(\frac{x_i^{var} - x_i^{rec}}{\sigma(x_i)} \right)^2 \tag{6.3}$$

is a simple χ^2-like term where correlations between parameters are not included[2] and where $\sigma(x_i)$ corresponds to the experimental inaccuracy of i-th parameter. A set of parameters $\mathbf{x}^{min}$ which minimizes the value of F in Equation 6.2 corresponds to these of values which satisfy the imposed constraints which at the same time are least varied with respect to original measurements.

6.1.2 Tuned parameters and physical constraints

The primary set of measured quantities whose improvement in accuracy is desired in the fit consists of spatial coordinates and times of the four EMC clusters which are used in the $\mathrm{K} \to \pi^0\pi^0$ vertex reconstruction. Two physical constraints on their values were devised and are listed below.

1. The position of reconstructed vertex must be consistent with the length of the trajectory of a kaon produced at the ϕ decay point and having a velocity υ_K. This constraint is similar to the third criterion for solution choice from Section 5.3 and takes the form:

   $$\mathrm{C}_0(\mathbf{x}) = \upsilon_K \, t - \mathrm{S}, \tag{6.4}$$

   where the path travelled by kaon between ϕ vertex V_ϕ before its decay in $\mathrm{V_K}$ point is:

   $$\mathrm{S} = |\mathrm{V_K} - \mathrm{V}_\phi|, \tag{6.5}$$

[1] As an example constraint, $m_{\pi^0}^{var} - m_{\pi^0}^{PDG} = 0$ may be given, where the *var* superscript denotes a varied reconstructed value of π^0 mass and $m_{\pi^0}^{PDG} = 134.9766 \pm 0.0006$ MeV/c^2 is the value recommended by PDG [5].

[2] As all variable parameters in the fit are independently measured in the detector, no significant correlations should exist.

for signal events. I case of regeneration, the path must be modified as it will be later described in Section 6.3. The cluster coordinates enter the above constraint indirectly through vertex reconstruction of kaon decay into $\pi^0\pi^0$. Moreover, as additional experimental values, spatial coordinates of ϕ meson decay point and kaon velocity, enter this constraint, they are also tuned as parameters in the fit.

2. Due to the fact that the four gamma quanta in the $K \to \pi^0\pi^0 \to 4\gamma$ process come from decays of the neutral pions, invariant masses of $\gamma\gamma$ pairs must equal be the mass of π^0. The $\gamma\gamma$ invariant mass of i-th pair is calculated as below:

$$M_i^{\gamma\gamma} = \sqrt{2E_{\gamma_{i,1}} E_{\gamma_{i,2}} \cos(1 - \theta_i)}, \tag{6.6}$$

where E_γ indicates the γ energy measured by EMC and θ is the angle between momentum vectors as indicated in Figure 6.1. In order to calculate the θ angle, the $K \to \pi^0\pi^0$ vertex must previously be reconstructed. Additionally, the use of cluster energies in the constraint motivates their inclusion as variable parameters in the fit. For each of the $\gamma\gamma$ pairs the penalty function is of the form:

$$\mathrm{C_i}(\mathbf{x}) = M_i^{\gamma\gamma} - m_{\pi^0}, \qquad i = 1, 2. \tag{6.7}$$

As the assignment of four neutral clusters into pairs is not initially known, a sum of the constraints in quadrature $\mathrm{C_1}^2(\mathbf{x}) + \mathrm{C_2}^2(\mathbf{x})$ is calculated for each of three possible pair combinations of which one is chosen that yields the smallest value of $\mathrm{C_1}^2(\mathbf{x}) + \mathrm{C_2}^2(\mathbf{x})$.

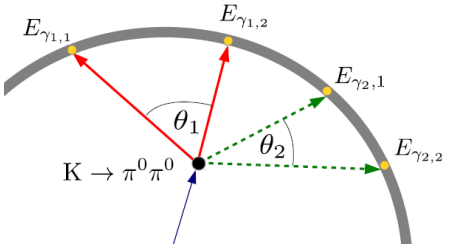

FIGURE 6.1: Angles between directions of paired gammas and their respective energies measured by the EMC, used to calculate invariant masses of $\gamma\gamma$ pairs. Red solid lines indicate one pair and green dashed – the second one.

In addition to the above physical constraints, several geometrical conditions were also imposed on the system to ensure that the reconstructed vertex does not lie outside limits of the detector and that during the variation of cluster coordinates the clusters are not shifted outside of the calorimeter. Penalties for violation of the geometrical constraints (proportional to the distance between the vertex or cluster position and the exceeded limit) are summed into a common penalty function $\mathrm{C_3}$:

$$C_3 = \sum_{clusters} \sum_{\substack{EMC \\ limits}} d_{clu,limit} + \sum_{\substack{detector \\ limits}} d_{vtx,limit}, \tag{6.8}$$

where $d_{x,limit}$ (with x being the location of a cluster or vertex) is defined as:

$$d_{x,limit} = \begin{cases} |\text{limit} - x| & \text{if x outside limit} \\ 0 & \text{if x inside limit} \end{cases} \tag{6.9}$$

After taking into account the quantities utilized in the constraints in addition to the input parameters of vertex reconstruction algorithm, all the variable parameters in the fit are as follows:

- cluster coordinates: $\mathrm{X_i}, \mathrm{Y_i}, \mathrm{Z_i}, \mathrm{T_i}$ for $i = 1, \ldots, 4$,
- ϕ decay point location: $\mathrm{x}_\phi, \mathrm{y}_\phi, \mathrm{z}_\phi$,
- kaon velocity υ_K,
- EMC cluster energies $\mathrm{E_i}$ for $i = 1, \ldots, 4$.

The above constitute a set of 24 variable parameters in the fit.

6.1.3 Minimization procedure

The minimum of the function F($\mathbf{x}$) introduced in Equation 6.2 can be found numerically using tools for multidimensional optimization. In this work the *Migrad* minimizer from the MINUIT package [38] was used. The minimizer varies the values of parameters in an allowed range and computes the value of a given function F in order to find a set $\mathbf{x}^{min}$ which minimizes F.

The constraints introduced in Section 6.1.2 (and thus also the minimized function F) depend on the location of the reconstructed vertex. Therefore the reconstruction is conducted in each iteration of the minimizer using the varied parameters $\mathbf{x}^{var}$. However, as reconstruction yields two solutions for the vertex, none of which can be discriminated at that point, the minimization is performed twice each time using a different solution for the vertex.

Algorithm 6.1 presents the flow of reconstruction with the fit performed for a single event. First, *Migrad* is called to find a set of parameters $\mathbf{x}_1$ which minimizes the function F being in a general form as in Equation 6.2 (exact forms of the functions used will be described later) where solution 1 is always chosen as the decay vertex in its reconstruction. Next, the same is done always using solution 2 and the minimum $\mathbf{x}_2$ is found. It should be noted, however, that the minimizer is not always able to converge to a proper minimum. In case no minimum is found for one of the solutions, it is assumed that this solution is non-physical and it was not possible to find a set of parameters which satisfy the constraints well. The other solution is then chosen as describing the physical vertex. For some events

Data: initial set of parameters $\mathbf{x}_0$ for an event
Result: vertex
`Minimize(`$\mathbf{x}_0$`)` using solution 1 $\rightarrow \mathbf{x}_1$
`Minimize(`$\mathbf{x}_0$`)` using solution 2 $\rightarrow \mathbf{x}_2$
if *both minimizations converged* **then**
  `Reconstruct(`$\mathbf{x}_1$`)` using solution 1 $\rightarrow$ vertex 1
  `Reconstruct(`$\mathbf{x}_2$`)` using solution 2 $\rightarrow$ vertex 2
  if $|\upsilon\, t_i - \mathrm{S}_i| < 1$ *cm for only one vertex of* i *=1,2* **then**
    vertex $\leftarrow$ vertex for which $|\upsilon\, t_i - \mathrm{S}_i| < 1$
  else if $\chi^2(\mathbf{x}_1) \leq \chi^2(\mathbf{x}_2)$ **then**
    vertex $\leftarrow$ vertex 1
  else
    vertex $\leftarrow$ vertex 2
else if *only one of minimizations converged* **then**
  vertex $\leftarrow$ result for the solution whose minimization converged
else
  vertex $\leftarrow \emptyset$

ALGORITHM 6.1: Procedure applied to each event in order to select the proper solution for the vertex and reconstruct the vertex using input parameters tuned by the fit.

it may happen that use of neither of the solutions leads to a good minimum. The vertex is not reconstructed for these events.

Most often, however, minimizations using both solutions converge to a minimum (about 67.7% events). The vertex reconstruction is then performed for both solutions, each time utilizing the respective set of minimizing parameters $\mathbf{x}_{1,2}$. The two vertices obtained this way are then checked to satisfy the $\upsilon\, t_i - \mathrm{S}_i \approx 0$ criterion with a precision better than 1 cm and if only one solution satisfies this criterion then it is chosen. For a high number of events this criterion is well satisfied by both solutions and then the one is selected for which finding a minimum required a smaller variation of the initial parameters (which corresponds to a smaller χ^2 value). This is motivated by the fact that even for an artifact solution the optimization may find the parameters which minimize the $\upsilon\, t_i - \mathrm{S}_i$ difference, although at a cost of a huge change of the measured parameter values. The physical solution, however, should already be close to the minimum before variation.

A detailed formula of the minimized function (of a general form given in Equation 6.2) with the penalty functions of physical constraints normalized by the respective σ_j factors, reads:

$$\mathrm{F}(\mathbf{x}^{var}) = \chi^2(\mathbf{x}^{var}) + \sum_{j=0}^{2} \frac{\mathrm{C}_{\mathrm{j}}^2(\mathbf{x}^{var})}{\sigma_j} + 10^6 \times \mathrm{C}_3(\mathbf{x}^{var}), \tag{6.10}$$

where $\mathrm{C}_{0,1,2,3}$ are the penalty functions defined in Section 6.1.2 and $\sigma_{0,1,2}$ are the errors of determination of physical quantities used in the constraints (kaon path and time difference $\upsilon t - S$ for the first and the neutral pion mass reconstructed from a $\gamma\gamma$ pair for the second constraint). These errors were estimated using reconstructed Monte Carlo events. The sum of geometrical constraints is multiplied by a large factor as it is a simple penalty needed to keep the minimizer inside the allowed parameter phase space.

Each of the 24 variable parameters was allowed to be shifted from the originally measured value by no more than $3\sigma(x_i)$ where $\sigma(x_i)$ is the resolution of the i-th measured parameter. In case of parameters with an energy-dependent resolution (see Table 3.3), the σ values were calculated for each event using appropriate cluster energies. The performance of the fit was also tested with a smaller allowed variability of parameters equal to $1\sigma(x_i)$. Better results were, however, obtained with the 3σ variability as it will be shown in the next section.

At the first approach the *Migrad* tool was called once to find a minimum of function from Equation 6.10 for each of the solutions. When the new vertex reconstruction with fit was applied to the reconstructed MC events it was, however, observed that the optimization is not convergent to a minimum for a noticeable number of events. The exact statistics are given in Table 6.1. In case of a considerable fraction of the events only a minimization for one of the solutions was successful in finding a proper minimum (with a higher number of successes for the first solution). It was also possible that no minimum was found for any of the solutions in which case the fit could not be used to tune the input parameters of vertex reconstruction.

solutions with good minima	percentage of events
both solutions	67.7%
only solution 1	16.3%
only solution 2	7.4 %
none	8.6 %

TABLE 6.1: Percentage of minimizations convergent to a good minimum obtained with a single *Migrad* run.

An examination of the problem led to an observation that the $v\,t_i - \mathrm{S}_i$ penalty function (C_0) introduces strong correlations between parameters into the minimized function F. Unfortunately, as the input parameters enter the $v\,t_i - \mathrm{S}_i$ difference through the complicated reconstruction as in Appendix A, it is difficult to take such correlations into account or to remove them. Moreover, this problem cannot be easily parametrized differently. Therefore it was chosen to perform the minimizations iteratively with the constraints applied with weights increased between minimizations. This approach follows a scheme of an iterative method with quadratic penalty functions as described in Ref. [39].

For use with this method, the F function was formulated as follows:

$$\mathrm{F}(\mathbf{x}^{var}, \mu) = \chi^2(\mathbf{x}^{var}) + \sum_{j=0}^{3} \mu_j \mathrm{C}_\mathrm{j}^2(\mathbf{x}^{var}), \tag{6.11}$$

where the μ_j coefficients are weights of each of the constraints. The whole minimization procedure is summarized in Algorithm 6.2. Initially, the weights are set to small values in order to avoid strong correlations of parameters due to constraint functions. Then a

series of subsequent minimizations is performed with *Migrad*, each time using the minimum resulting from previous minimization as a starting point. Between each two calls to *Migrad*, weights are increased by an order of magnitude thus imposing the constraints more strictly. If after several iterations the minimization does not converge to a proper minimum, the result of last successful attempt is used as the minimum. Otherwise a fixed number of iterations $n_{max} = 10$ is performed.

Data: initial set of parameters $\mathbf{x}^{(0)}$, $\mu^{(0)}$ – initial penalty weights
Result: $\mathbf{x}^{min}$ – set of parameters minimizing $FCN(\mathbf{x}^{min}, \mu)$
i $\leftarrow$ 0
repeat
  $\mathbf{x}^{(i+1)} \leftarrow$ `Minimize(`*FCN(*$\mathbf{x}^{(i)}$, $\mu^{(i)}$*)*`)`
  $\mu^{(i+1)} \leftarrow \mu^{(i)} \cdot 10$
  i $\leftarrow$ i+1
until *last minimization convergent* **or** $i = n_{max}$;
if *last minimization convergent* **then**
  $\mathbf{x}^{min} \leftarrow \mathbf{x}^{(i+1)}$
else
  $\mathbf{x}^{min} \leftarrow \mathbf{x}^{(i)}$

Algorithm 6.2: Procedure of iterative minimizations using quadratic penalty functions. "Minimize" represents calls to the *Migrad* minimizer. The weights μ of each constraint are increased between subsequent minimizations by an order of magnitude. If minimization fails to converge, the last proper minimum found is taken as the result.

Such an iterative minimization solved the problem of unsuccessful searches for the minimum as shown in Table 6.2. The results of input parameter tuning using this method are presented in the next section.

solutions with good minima	percentage of events
both solutions	96.8%
only solution 1	3.0%
only solution 2	0.2%
none	0.0%

Table 6.2: Percentage of minimizations convergent to a good minimum obtained with the iterative method. The minimization is always successful for at least one of the solutions.

6.2 Results of input parameter tuning

In Section 5.4.2 the results of $K \to \pi^0\pi^0$ decay vertex reconstruction were shown for the case of reconstructed MC events where the experimental uncertainty of reconstruction input data renders it impossible to use the $v\,t_i - S_i \approx 0$ criterion in order to extract a physical solution (see Figure 5.4). The aim of first constraint used in the fit (see Section 6.1.2), based on the same physical requirement, was to tune the measured values so that this

relation is satisfied. The plots in Figure 6.2 present a distribution of the same quantities as in Figure 5.4 but obtained from vertex reconstruction with tuned parameters (with 3σ parameter variability during the fit). This result shows that the aim was achieved since for a majority of events at least one of the $v\,t_i - \mathrm{S}_i$, $i = 1, 2$ differences is close to zero, similarly as in case of generated MC events (Figure 5.2).

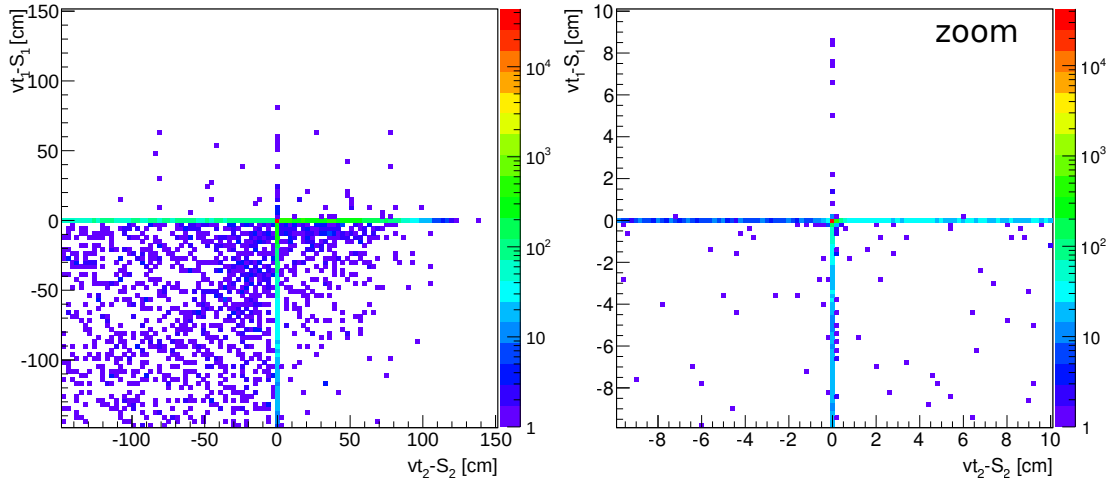

FIGURE 6.2: The first physical constraint after tuning the parameters by means of a fit. Left: two-dimensional distribution of the $v\,t_i - \mathrm{S}_i$ values for solutions 1 and 2 obtained in the vertex reconstruction using tuned parameters. Right: the left-side distribution zoomed for $|v\,t_i - \mathrm{S}_i| < 10$ cm.

The fit was tested with two allowed ranges of parameter variability — 1σ and 3σ around the measured value. Although the above result was obtained with the 3σ allowed variability, the use of smaller variable range yields a similar result. However, a detailed consideration of each of the one-dimensional $v\,t_i - \mathrm{S}_i$ distributions shown in Figure 6.3 reveals that in the second case the distributions are broader, indicating worse performance of the fit. Nonetheless in both cases it can be stated that the first physical criterion of the fit is satisfied with a precision of the order of 1 mm.

The degree to which the second physical constraint of the fit is satisfied can be assessed using the distribution of invariant masses of $\gamma\gamma$ pairs obtained with the reconstructed neutral vertices. Such distributions resulting from fits with the two tested parameter variable ranges are shown in Figure 6.4. The fact that distributions are peaked at the precise value of π^0 mass as expected for photons coming from neutral pion decays as well as small width of the peaks prove that the second physical constraint is also well satisfied. Again, however, a slightly worse result is observed for the 1σ version.

In Figure 6.5 distributions of χ^2 values obtained with the tuned parameters are shown. They may be treated as a measure of how strongly the parameters were varied in the fit with respect to their measured values. Left-side plot presents the result of fit with 3σ variability and right-side plot — of 1σ variability. It should be noted that a maximal

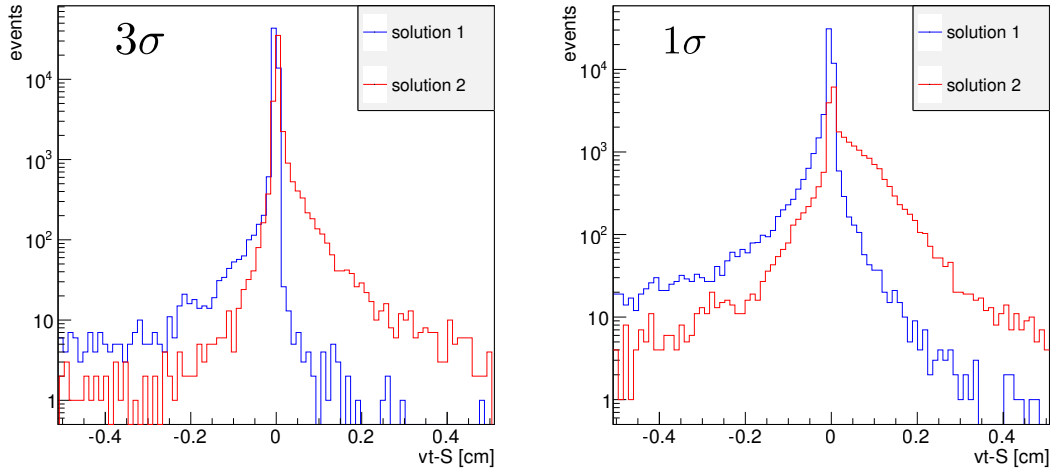

FIGURE 6.3: One-dimensional distributions of $v\,t_i - \mathrm{S}_i$ values for solutions 1 and 2 obtained after tuning the reconstruction input parameters with a fit with parameter variability of 3σ (left plot) and 1σ (right plot) around the measured value. The distribution obtained with smaller variability of parameters is noticeably broader.

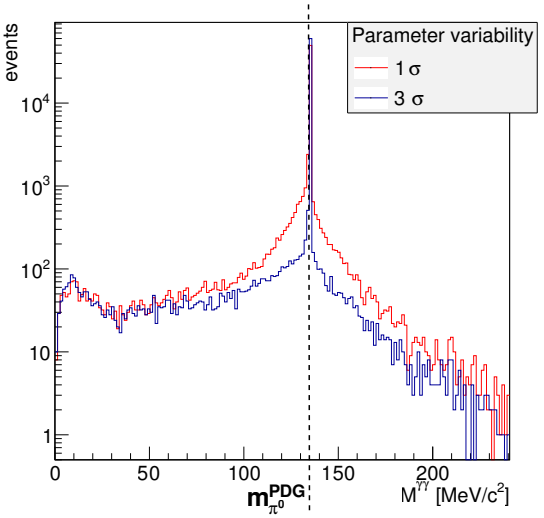

FIGURE 6.4: Distribution of the invariant masses of $\gamma\gamma$ pairs obtained with tuned parameters after the fit variants with two different parameter variability ranges. Dashed vertical line corresponds to the value of π^0 mass according to PDG [5].

possible variation of a single parameter contributes to the χ^2 a value of $\frac{(3\sigma)^2}{\sigma^2} = 9$ in the former and respectively 1 in the latter case which is the reason for the distributions terminating respectively at 9·24=216 and 24. Peaks appearing at ends of both distributions correspond to events where all parameters were shifted by the minimizer to the end of their allowed phase space. This shows that unfortunately even though the minimizer may signal finding a proper minimum, it may not be a physically valid one. It is also visible that such a peak is significantly larger with respect to the peak of lower χ^2 values (which correspond to small variation of parameters) in case of 1σ variability which is an indication that this

variability range is too narrow to search for minimizing values of parameters. Therefore, in further considerations the 3σ variant was used. Other peaks visible in both distributions in Figure 6.5 correspond to events where the values of a certain number of parameters were moved to the edge of allowed range during minimization. Numbers of parameters for which this happens are 19 and 22 (in the left distributions these appear as peaks at 171 and 198 respectively). Although this fact suggests that it is not equally easy to find a minimizing value in each of the fit parameters, the groups of parameters which are maximally varied in the above cases were not identified.

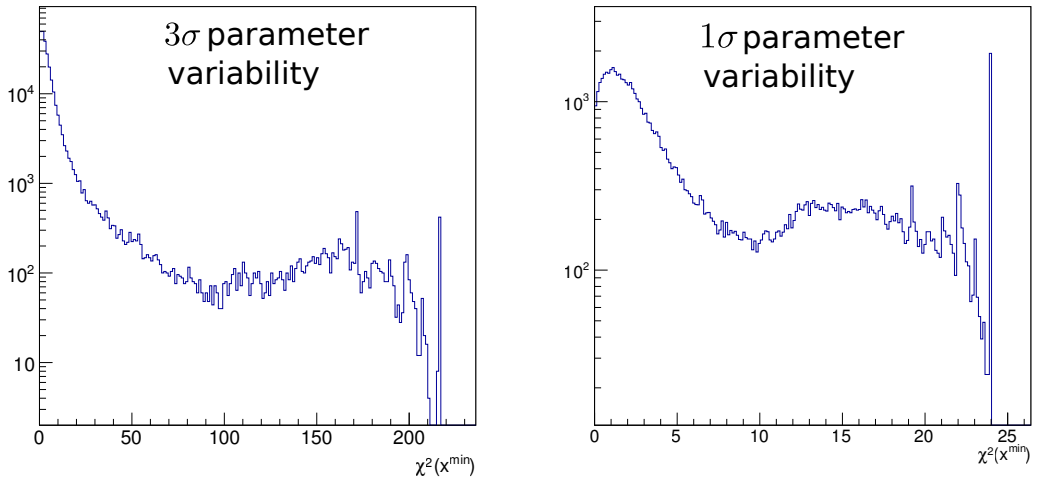

FIGURE 6.5: Distributions of the χ^2 (see Equation 6.3) values from fit with parameter variability of 3σ (left plot) and 1σ (right plot). Peaks at the ends of distributions correspond to events where all parameters were varied to the maximal allowed degree by the minimizer. A larger fraction of such events in case of 1σ variability indicates this variable range is too narrow. Other peaks appearing at 19 and 22 in the right plot correspond to peaks at 171 and 198 in the left plot and originate from events where a certain number of parameters was maximally varied which shows that some groups of parameters are more difficult to find minimizing values than the others.

Finally, the reconstructed quantities from MC events, tuned by the fit, were used to estimate the spatial resolution of neutral vertex reconstruction. The result is shown in Figure 6.6. For vertices distant from the ϕ decay vertex a threefold improvement in accuracy was achieved with respect to the resolution without the fit (Figure 5.5) whereas closer to ϕ the improvement is significantly higher. From the point of view of rejection of kaon regeneration background the spatial vertex resolution is of special importance in the region about 10 cm from the detector center where the spherical beam pipe is located and thus where the regeneration process occurs, spoiling the Δt distribution (see Figure 4.4). The vertex accuracy in this region is estimated to be about 2.5 cm.

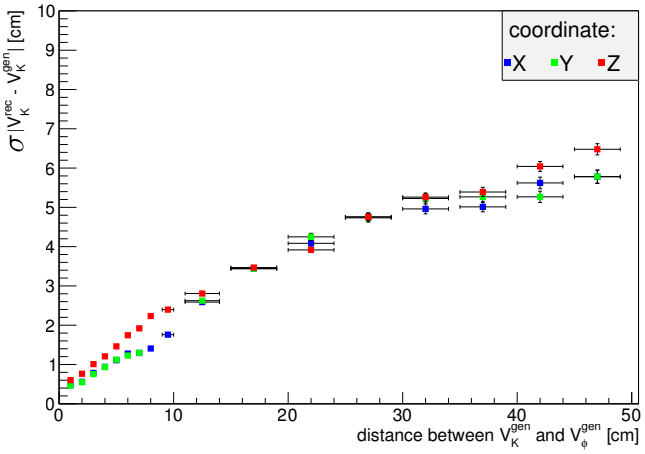

FIGURE 6.6: Spatial resolution of the neutral vertex reconstruction as a function of vertex distance from the ϕ decay point. Resolution for each coordinate is shown separately as indicated in the legend. This result was obtained with vertex reconstruction including input parameter tuning. A considerable improvement is visible with respect to the resolution without the fit (Figure 5.5).

6.3 Tuning the parameters with regeneration assumption

One of the criteria for selecting a proper solution from Section 5.3 as well as the first constraint in the fit are based on a comparison of the path travelled by kaon and the product of its flight time and velocity. In the form presented until now, the kaon path was always calculated as a simple distance between the ϕ decay point and the reconstructed kaon decay vertex. As it can be easily seen in Figure 4.8, this scheme does not correspond to the physical situation of events with incoherent regeneration. Because of implicitly assuming no regeneration in an event, using this form of distance S in the fit will be referred to as fitting with signal assumption in the remainder of this work.

In order to make the constraint $\upsilon\, t_i - \mathrm{S}_i \approx 0$ well applicable to the case of regeneration, an alternative version of the fit was prepared which assumes regeneration in an event. Idea of the modification is presented in the left side of Figure 6.7. Rather being the direct distance (grey dotted arrow), the path travelled by a kaon before decay is calculated as a sum of lengths of two segments. First of them ($\mathrm{S_a}$), is the distance travelled by the original $\mathrm{K_L}$ before it undergoes regeneration in point P. Although location of this point is not known for an event, it may be safely assumed to lie along the $\mathrm{K_L}$ momentum direction obtained with the tagging decay $\mathrm{K_S} \to \pi^+\pi^-$. The second segment of length S_b spans between the regeneration point and the $\mathrm{K_L} \to \pi^0\pi^0$ decay vertex. As regeneration usually changes the direction of kaon flight, these two segments form an angle θ corresponding to the regeneration angle estimated in Section 4.2.

An important fact for using the constraint $\upsilon t_i - (\mathrm{S_a} + \mathrm{S_b}) \approx 0$ in the fit for events with regeneration on the beam pipe is that momentum value of the regenerated kaon does not differ from the one of original $\mathrm{K_L}$ by more than 10%. Therefore the comparison of length of

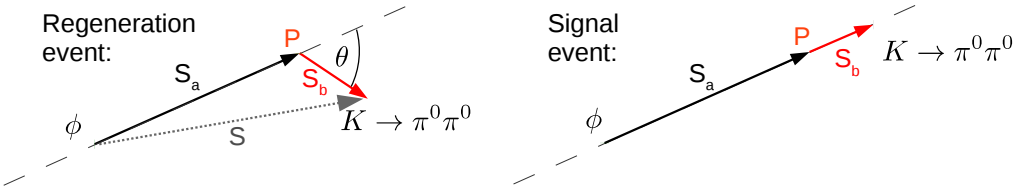

FIGURE 6.7: Scheme of the kaon path length calculation with the assumption of regeneration taking place in point P along the fight direction of original long-lived kaon (dashed line). The path is a sum of sections S_a and S_b which form an angle θ. Left scheme presents the case of regeneration event when the true kaon path is different from the one calculated with signal assumption (dotted arrow). Right drawing presents the case of signal events where the two paths S and $S_a + S_b$ are equal.

S_b with the velocity of K_L rather than of regenerated K_S (which is not measured) accounts for an error in the $vt_i - (S_a + S_b)$ calculation not larger than 1 mm$\times\frac{t}{\tau_s}$.

Location of the regeneration point P for each event may be estimated using the roughly known position of vertex. If it lies in an area around one of the main regenerating materials in KLOE and the regeneration occurs, it predominantly happens inside this material. Therefore an intersection of the original kaon momentum direction and surface of a certain regenerating material is taken as the P point. In further considerations, only the case of assuming regeneration on the spherical beam pipe will be presented. The material is then a sphere of 100 mm radius whose 500 μm thickness may be neglected with the accuracy available.

Since the θ angle is about 60^o for most of the regeneration events (except on the DC wall), the difference in kaon path calculated as S and as $S_a + S_b$ is expected to be:

$$\Delta S = (S_a + S_b) - S = (S_a + S_b) - \sqrt{S_a^2 + S_b^2 - 2S_a S_b cos(\pi - \theta)}, \qquad (6.12)$$

which for the case of regeneration on the BP ($S_a \approx 100$ mm), $\theta = 60^0$ and the regenerated K_S living τ_S ($S_b = \lambda_s \approx 6$ mm) is about 2.88 mm.

As the fit usually minimizes the $v\,t_i - S_i$ value with a precision better than 1 mm, such a difference can change the result significantly when the version with signal assumption is applied to a regeneration event. Conversely, taking the regeneration assumption should not disturb the fit of a signal event because the S_a S_b segments are co-linear in this case as shown in the right of Figure 6.7.

The above observations reveal a potential of distinguishing regeneration from signal events using the quality of the two versions of the fit which will be described in the next chapter.

Chapter 7

Application of the new reconstruction method

Tests of neutral vertex reconstruction including tuning of the input parameters with the fit have shown that spatial resolution of vertices located in the region around the spherical beam pipe (which contributes a large amount of regeneration events) is about 2.5 cm for each coordinate. Unfortunately, such accuracy is not sufficient for recognition of regeneration only by considering the position of reconstructed vertex since the mean path travelled by regenerated short-lived kaon is about 6 mm.

However, observation that incoherent regeneration is associated with a change in the length of path travelled by kaons before decay (as presented in Section 6.3) reveals a possibility of utilizing the fit constraint based on the $v\,t_i - \mathrm{S}_i$ difference in order to observe an influence of the aforementioned path difference on the fit quality. Such attempt to reject regeneration using the neutral vertex reconstruction with the fit will be described in this chapter.

7.1 Rejection of regeneration events

7.1.1 Possibilities of regeneration recognition

As explained in the previous chapter, two variants of the first fit constraint may be formulated — assuming that regeneration occurred in an event or not. In the latter case the calculation of distance S travelled by the kaon will not correspond to the physical situation if applied to an event with regeneration. The discrepancy between the length composed of two sections as in left scheme of Figure 6.7 and the direct distance between ϕ and K mesons decay points is expected to be of the order of several millimeters, i.e. significantly larger than the precision to which the $v\,t_i - \mathrm{S}_i \approx 0$ criterion is satisfied in the fit for signal events. Therefore it may be expected that application of fit with signal assumption to a regeneration event will result with the $v\,t_i - \mathrm{S}_i$ difference being more difficult to minimize.

Such a difficulty can manifest itself in two ways: the minimization procedure may find a minimum for which the first physical criterion is not satisfied well or the parameters $\mathbf{x}^{min}$ which properly minimize $v\,t_i - \mathrm{S}_i$ will be found, however at the cost of their large variation with respect to original values which will result in a large value of $\chi^2(\mathbf{x}^{min})$.

Conversely, the use of fit with the regeneration assumption in case of a regeneration event would lead to a minimization as feasible as when fit with signal assumption is applied to a signal event because the appropriate form of the kaon path length is properly taken into account. Moreover, taking the regeneration assumption in case of no regeneration in an event should not influence the performance of fit since the path calculated as sum of two sections should then be identical with the direct distance between ϕ and reconstructed kaon vertex (see right scheme of Figure 6.7).

7.2 Results

The three detector components described in Section 4.2 contribute a predominant part of all regeneration events in KLOE. Therefore, the attempts to reject regeneration are concentrated on areas where these elements are located. Precise knowledge of their position allows for the use of fit with regeneration assumption where the location of regeneration point is assumed to be inside the material.

In order to analyze differences of fit performance with and without regeneration assumption, the kaon neutral decay vertices located in regions around the regenerating materials may be considered, separately for each of the major regeneration sources in KLOE. The following tests used only events where the $\mathrm{K} \to \pi^0\pi^0$ vertex was in the limits of radial distance ± 1 cm from the spherical beam pipe, as shown in Figure 7.1. This region was chosen in order to investigate the regeneration process taking place in the beam pipe material.

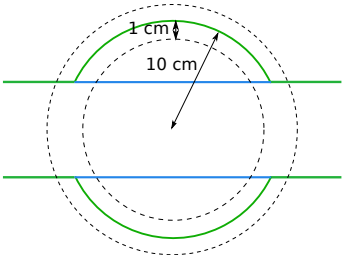

FIGURE 7.1: Region of 1cm width around the spherical beam pipe (green) where the $\mathrm{K} \to \pi^0\pi^0$ vertices were considered both with signal and regeneration assumption in the fit.

In order to determine the radial distance of vertex from the detector center, the vertex location reconstructed using the standard algorithm was used as being more accurate and as information on the deviation of vertex location from the original flight direction of the $\mathrm{K_L}$ is not relevant for the radial distance. In the sample used, the region of 1 cm

around the spherical beam pipe contained about 3200 signal events and 11700 events with regeneration. For each of these events the fit was first performed with a signal assumption and then independently a fit with regeneration point assumed to lie on the BP was carried out.

As mentioned in the previous section, the two observables resulting from the fit in which a discrepancy was expected to appear between results of fit with and without regeneration assumption applied to regeneration events are the $v\,t_i - \mathrm{S}_i$ distance for the physical solution and the $\chi^2(\mathbf{x}^{min})$ (see Equation 6.3) value for the set of parameters $\mathbf{x}^{min}$ which minimizes the physical constraints. In further considerations the *sig* and *reg* subscripts will denote values of these quantities obtained in the fit with signal and regeneration assumption, respectively.

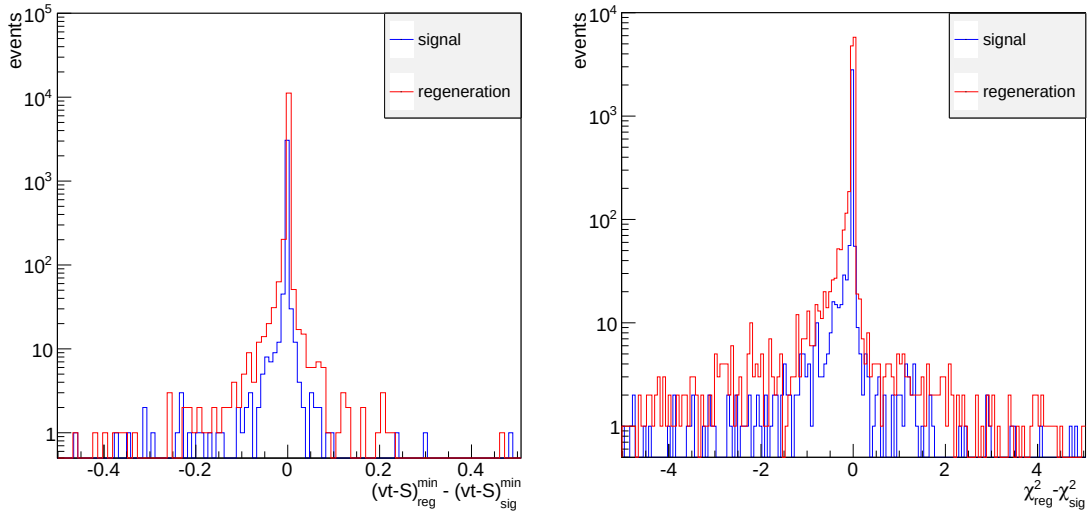

FIGURE 7.2: Left: distribution of differences between $v\,t_i - \mathrm{S}_i$ values obtained using a fit with (*reg* subscript) and without regeneration assumption (*sig* superscript). Right: distribution of differences between $\chi^2(\mathbf{x}^{min})$ (a measure of degree of parameter variation in the fit, see Equation 6.3) values obtained using a fit with and without regeneration assumption. The above distributions do not exhibit any significant discrepancy between signal and regeneration events.

Left plot of Figure 7.2 presents a distribution of differences between the $(v\,t_i - \mathrm{S}_i)$ values minimized with and without an assumption of regeneration in an event. It is visible that while both distributions are narrow, they do not differ to an extent that would allow to use the value of such difference for each event to discriminate regeneration background. Unfortunately, distribution of the second quantity expected to be useful, the difference between χ^2 values for the minima found with two variants of the fit, also does not exhibit any substantial discrepancy between signal and regeneration events as it can be seen on the right plot of Figure 7.2.

The values of the χ^2 which give a measure of the degree to which the parameters had to be varied in order to find a set of values minimizing the physical constraints, was expected to

be larger for regeneration events to which the signal assuming version of the fit is applied. The distribution shown in the right panel of Figure 7.2 is peaked at 0 which suggests that no systematic difference is observed. A two-dimensional distribution of these values presented with respect to each other as in the plot in Figure 7.3 (shown separately for signal and regeneration events) confirms that in most cases the χ^2 values yielded by both fit variants are similar. Although deviations from this occur, they are visible for both regeneration and signal events. Therefore, no possibilities to reject regeneration may be observed in the distributions of χ^2.

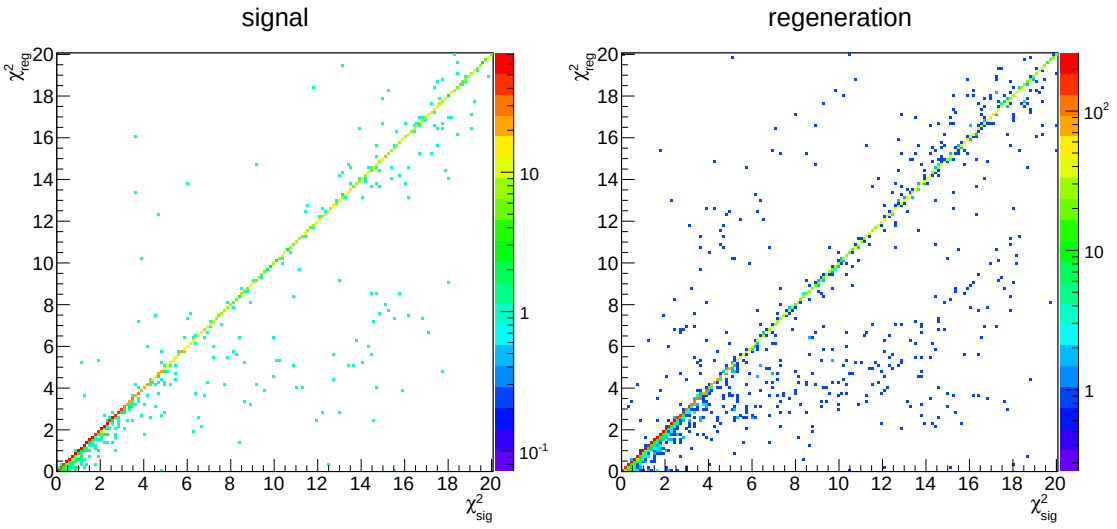

FIGURE 7.3: Two-dimensional distributions of the $\chi^2(\mathbf{x}^{min})$ values for the minima obtained with a fit with regeneration assumption (vertical axes) and with signal assumption (horizontal axes). Left-side plot corresponds to signal events only while right-side plot presents only regeneration events. Although there are events for which these two values are noticeably different, such cases occur for both signal and regeneration.

Traces of the regeneration can, however, also be expected to appear in the other observable: the value of $v\,t_i - \mathrm{S}_i$ difference minimized by the fit. As it was shown in the right-side plot of Figure 7.2, the bare difference of these values obtained with two fit variants does not show useful discrepancy between signal and regeneration either. It may then be useful to analyze relative behaviour of $v\,t_i - \mathrm{S}_i$ and χ^2. Figure 7.4 shows a set of two-dimensional distributions of these quantities for four cases of: signal-assuming fit applied to signal events (upper left) and to regeneration events (lower left) and fit with regeneration assumption applied to signal events (right) and to regeneration events (lower right).

Unfortunately, The above distributions exhibit no differences significant enough to be used to devise cuts which would allow for rejection of a part of regeneration events with no simultaneous effect on the signal events. This is probably a result of the insufficient accuracy of determination of neutral vertex spatial coordinates by the new reconstruction algorithm. As concluded in Chapter 6, in the region around the spherical beam pipe the standard deviation of distances between reconstructed and generated $\mathrm{K_L} \to \pi^0\pi^0$ vertex is about 2.5 cm for each spatial coordinate. Therefore, the inaccuracies involved in both

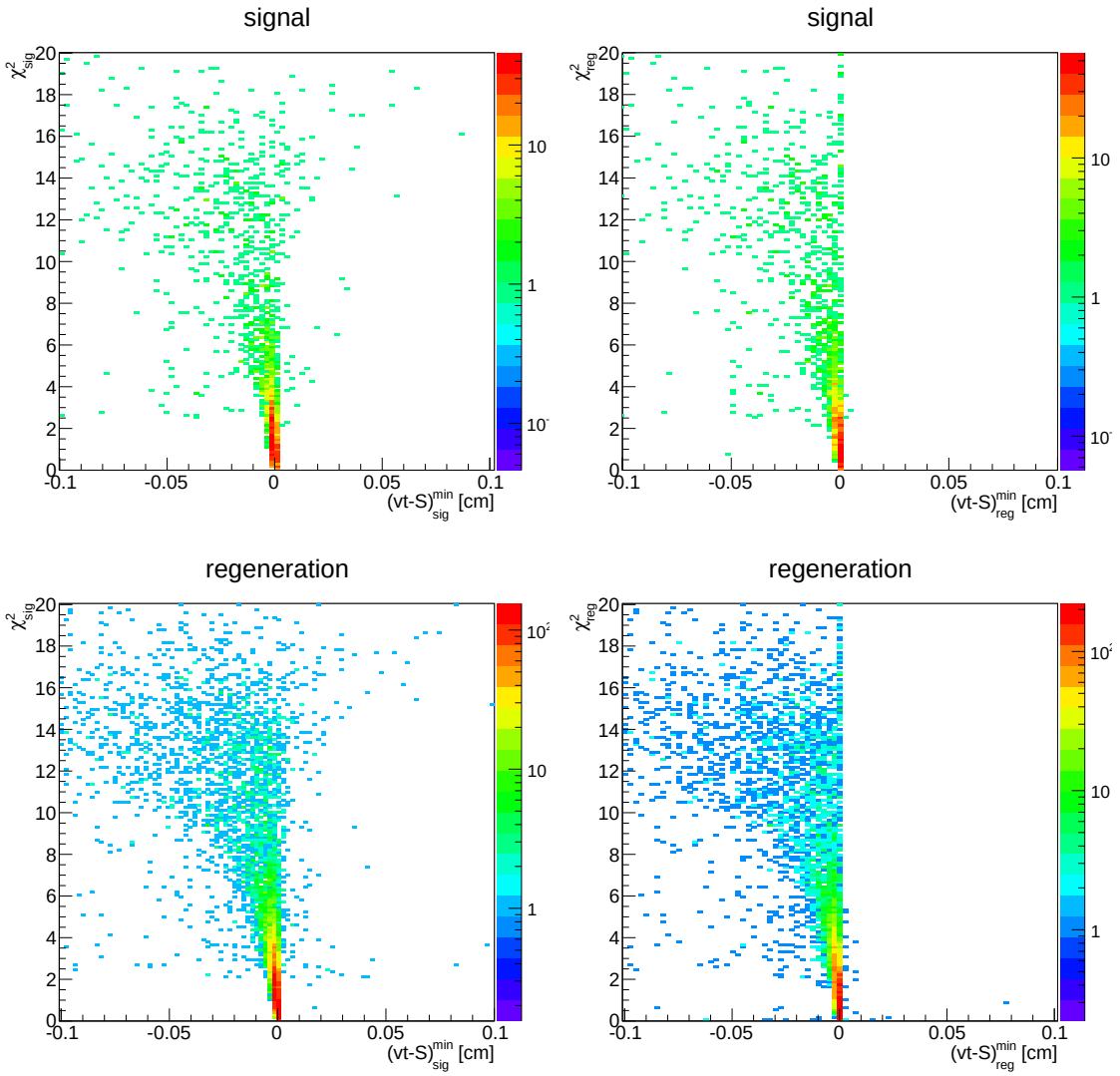

FIGURE 7.4: Two-dimensional distributions of the χ^2 value after the fit and the $v\,t_i - \mathrm{S}_i$ difference as minimized by this fit. Two plots in the left column present the distributions of these quantities obtained with a fit with signal assumption and the plots from right columns – with regeneration assumption. Plots in the upper row were obtained with signal events only, and lower plots – with events with regeneration.

variants of the fit procedure are larger than effect of wrong kaon path calculation which appears in case of applying a signal-assuming fit to a regeneration event. In consequence, this effect is not distinguishable in the distributions presented above. This leads to the conclusions concerning applicability of the new reconstruction method to regeneration rejection, which will be presented in the next chapter.

Chapter 8

Conclusions

This work aimed at an elaboration of a new method of reconstruction of the $K \to \pi^0\pi^0$ decay vertex for the KLOE experiment. Reconstruction was required not to assume the neutral vertex to lie along momentum direction of the original kaon produced in a ϕ meson decay and thus to account for the possibility of kaon regeneration.

Such a method using four calorimeter clusters originating from photons created in π^0 decays and based on an intersection of sets of possible photon origin points was invented. It was implemented and proved to find the vertex location correctly using Monte Carlo generated events. However, the vertex resolution for MC reconstructed events was discovered to be insufficient due to inaccuracies of reconstructed cluster coordinates which are treated as reconstruction input.

In order to improve the accuracy of reconstructed neutral vertex location, the reconstruction algorithm was extended to involve a procedure of tuning the measured parameters by means of a kinematic fit. The fit was based on two constraints that a physical $K \to \pi^0\pi^0$ decay vertex must satisfy (the kaon meson must reach the origin point of four photons within a given time and invariant masses of two pairs of gammas must be equal to π^0 mass). An iterative multidimensional minimization method with quadratic penalty functions was employed.

The application of parameter tuning with the fit led to an enhancement in the resolution of neutral vertex spatial location with the improvement being especially large in case of vertices close to the ϕ meson decay vertex. Final resolution obtained with the new reconstruction algorithm is about 0.5 cm in each spatial coordinate for kaons decaying very close to their production point. In the region of spherical beam pipe location in KLOE (which is important for regeneration rejection) the kaon decay point can be determined with an accuracy of about 2.5 cm

Since the mean path travelled by a regenerated short-lived kaon in KLOE is about 6 mm, the above spatial vertex resolution is not sufficient for kaon regeneration in an event

to be visible in the vertex location with respect to the original kaon flight direction. Therefore other methods of recognition of regeneration background were sought for, using the comparison of quality of physical constraints minimization for signal and regeneration events with and without the regeneration assumption as presented in Chapter 7.

Calculations of the error in kaon path length resulting from treating an event with regeneration as a signal one yield a value substantially larger than the accuracy with which the $\upsilon\, t_i - \mathrm{S}_i \approx 0$ criterion is satisfied. Although this suggests that a difference in the fit quality of two fit variants should appear for regeneration events, no significant discrepancy was observed in the tests with MC reconstructed events. This is probably a result of the large inaccuracy of vertex determination which leads to the locations of neutral decay vertices which do not correspond well to the ideal case of kaon path calculation. With the present resolution of the new method the vertex may be reconstructed (in the region of the spherical beam pipe) in a distance of about 2.5 cm from the flight direction of original $\mathrm{K_L}$ even in case of signal events as this would result only from the uncertainty of reconstruction. In such a case the path travelled by the kaon before decay would differ from the real path length significantly despite no regeneration in the event. The above considerations lead to a conclusion that for the difference in fit quality between signal and regeneration events to be observable, the accuracy of the vertex spatial location determined by the new algorithm should be improved.

Although it could be concluded that with its present performance the $\mathrm{K} \to \pi^0\pi^0$ decay vertex reconstruction method presented in this work does not provide spatial resolution sufficient for rejection of regeneration background in the $\phi \to \mathrm{K_S K_L} \to (\mathrm{K_S K_S} \to)\pi^+\pi^-\pi^0\pi^0$ process at KLOE, the elaborated algorithm can be used as an alternative method for determination of other neutral vertices with sufficient number of photons, for example $\mathrm{K_L} \to 3\pi^0$.

Appendix A

Solution of the 4 spheres' intersection equation system

As mentioned in section 5.2 the system of quadratic equations describing the spheres constituted by sets of possible origin points of the γ paths for each of the four EMC clusters in the $K_L \to \pi^0\pi^0 \to 4\gamma$ decay can be written as follows:

$$(T_1 - t)^2 c^2 = (X_1 - x)^2 + (Y_1 - y)^2 + (Z_1 - z)^2, \tag{A.1}$$

$$(T_2 - t)^2 c^2 = (X_2 - x)^2 + (Y_2 - y)^2 + (Z_2 - z)^2, \tag{A.2}$$

$$(T_3 - t)^2 c^2 = (X_3 - x)^2 + (Y_3 - y)^2 + (Z_3 - z)^2, \tag{A.3}$$

$$(T_4 - t)^2 c^2 = (X_4 - x)^2 + (Y_4 - y)^2 + (Z_4 - z)^2, \tag{A.4}$$

where x, y, z and t are unknowns, c is the speed of light and capital letters denote the spatial and temporal coordinates of the clusters.

If the quadratic terms in the above equations are expanded, subtraction of any of these equations from another results in the elimination of all terms with the unknowns squared, i.e. x^2, y^2, z^2 and t^2. This way linear (in terms of the unknowns) equations may be obtained. At maximum three linearly independent equations can be produced by subtracting respective pairs of equations (A.1)–(A.4).

For the following considerations let us choose to subtract equations (A.2)–(A.4) from (A.1). The system of linear equations of then of the form:

$$\begin{aligned}
&-2x(\mathrm{X}_1-\mathrm{X}_2)-2y(\mathrm{Y}_1-\mathrm{Y}_2)-2z(\mathrm{Z}_1-\mathrm{Z}_2)-\mathrm{X}_1^2-\mathrm{X}_2^2+\mathrm{Y}_1^2-\mathrm{Y}_2^2+\mathrm{Z}_1^2-\mathrm{Z}_2^2 \\
&\qquad = -2c^2t(\mathrm{T}_1-\mathrm{T}_2)+c^2(\mathrm{T}_1^2-\mathrm{T}_2^2), \qquad \text{(A.5)} \\
&-2x(\mathrm{X}_1-\mathrm{X}_3)-2y(\mathrm{Y}_1-\mathrm{Y}_3)-2z(\mathrm{Z}_1-\mathrm{Z}_3)-\mathrm{X}_1^2-\mathrm{X}_3^2+\mathrm{Y}_1^2-\mathrm{Y}_3^2+\mathrm{Z}_1^2-\mathrm{Z}_3^2 \\
&\qquad = -2c^2t(\mathrm{T}_1-\mathrm{T}_3)+c^2(\mathrm{T}_1^2-\mathrm{T}_3^2), \qquad \text{(A.6)} \\
&-2x(\mathrm{X}_1-\mathrm{X}_4)-2y(\mathrm{Y}_1-\mathrm{Y}_4)-2z(\mathrm{Z}_1-\mathrm{Z}_4)-\mathrm{X}_1^2-\mathrm{X}_4^2+\mathrm{Y}_1^2-\mathrm{Y}_4^2+\mathrm{Z}_1^2-\mathrm{Z}_4^2 \\
&\qquad = -2c^2t(\mathrm{T}_1-\mathrm{T}_4)+c^2(\mathrm{T}_1^2-\mathrm{T}_4^2). \qquad \text{(A.7)}
\end{aligned}$$

In order to simplify the notation let us introduce the auxiliary parameters:

$$\begin{aligned}
\Delta\mathrm{X}_{\mathrm{ij}} &:= 2(\mathrm{X}_\mathrm{i}-\mathrm{X}_\mathrm{j}), \\
\Delta\mathrm{Y}_{\mathrm{ij}} &:= 2(\mathrm{Y}_\mathrm{i}-\mathrm{Y}_\mathrm{j}), \\
\Delta\mathrm{Z}_{\mathrm{ij}} &:= 2(\mathrm{Z}_\mathrm{i}-\mathrm{Z}_\mathrm{j}), \qquad \text{(A.8)} \\
\Delta\mathrm{T}_{\mathrm{ij}} &:= -2c^2(\mathrm{T}_\mathrm{i}-\mathrm{T}_\mathrm{j}), \\
\mathrm{C}_{\mathrm{ij}} &:= -c^2(\mathrm{T}_\mathrm{i}^2-\mathrm{T}_\mathrm{j}^2)+\mathrm{X}_\mathrm{i}^2-\mathrm{X}_\mathrm{j}^2+\mathrm{Y}_\mathrm{i}^2-\mathrm{Y}_\mathrm{j}^2+\mathrm{Z}_\mathrm{i}^2-\mathrm{Z}_\mathrm{j}^2,
\end{aligned}$$

where i, j are the indices numbering the EMC clusters and their corresponding equations from the initial system. These additional parameters are only dependent on the known values. The system of equations (A.5)–(A.7) can be then written in the form:

$$\begin{pmatrix} \Delta\mathrm{T}_{12} & \Delta\mathrm{X}_{12} & \Delta\mathrm{Y}_{12} & \Delta\mathrm{Z}_{12} \\ \Delta\mathrm{T}_{13} & \Delta\mathrm{X}_{13} & \Delta\mathrm{Y}_{13} & \Delta\mathrm{Z}_{13} \\ \Delta\mathrm{T}_{14} & \Delta\mathrm{X}_{14} & \Delta\mathrm{Y}_{14} & \Delta\mathrm{Z}_{14} \end{pmatrix} \begin{pmatrix} t \\ x \\ y \\ z \end{pmatrix} = \begin{pmatrix} \mathrm{C}_{12} \\ \mathrm{C}_{13} \\ \mathrm{C}_{14} \end{pmatrix}. \qquad \text{(A.9)}$$

As there are three equations and four unknowns in the system, an explicit solution cannot be directly found. Three of the unknowns, however, may be determined with the fourth one as a variable parameter. Let us choose the time t to be the parameter. In such a case the solution for $(x, y, z)(t)$ is of the form describing a parametric line in a three-dimensional space:

$$\begin{pmatrix} x(t) \\ y(t) \\ z(t) \end{pmatrix} = \begin{pmatrix} a_1 \\ a_2 \\ a_3 \end{pmatrix} \cdot t + \begin{pmatrix} b_1 \\ b_2 \\ b_3 \end{pmatrix}, \qquad \text{(A.10)}$$

where a_i and b_i are defined as below:

$$\begin{aligned}
a_1 =&(\Delta T_{14}\Delta Y_{13}\Delta Z_{12} - \Delta T_{13}\Delta Y_{14}\Delta Z_{12} - \Delta T_{14}\Delta Y_{12}\Delta Z_{13} \\
&+ \Delta T_{12}\Delta Y_{14}\Delta Z_{13} + \Delta T_{13}\Delta Y_{12}\Delta Z_{14} - \Delta T_{12}\Delta Y_{13}\Delta Z_{14})/d, \\
a_2 =&(-\Delta T_{14}\Delta X_{13}\Delta Z_{12} + \Delta T_{13}\Delta X_{14}\Delta Z_{12} + \Delta T_{14}\Delta X_{12}\Delta Z_{13} \\
&- \Delta T_{12}\Delta X_{14}\Delta Z_{13} - \Delta T_{13}\Delta X_{12}\Delta Z_{14} + \Delta T_{12}\Delta X_{13}\Delta Z_{14})/d, \\
a_3 =&(\Delta T_{14}\Delta X_{13}\Delta Y_{12} - \Delta T_{13}\Delta X_{14}\Delta Y_{12} - \Delta T_{14}\Delta X_{12}\Delta Y_{13} \\
&+ \Delta T_{12}\Delta X_{14}\Delta Y_{13} + \Delta T_{13}\Delta X_{12}\Delta Y_{14} - \Delta T_{12}\Delta X_{13}\Delta Y_{14})/d,
\end{aligned} \tag{A.11}$$

$$\begin{aligned}
b_1 =&(B1(\Delta Y_{13}\Delta Z_{14} - \Delta Y_{14}\Delta Z_{13}) + B2(\Delta Y_{14}\Delta Z_{12} - \Delta Y_{12}\Delta Z_{14}) \\
&+ B3(\Delta Y_{12}\Delta Z_{13} - \Delta Y_{13}\Delta Z_{12}))/d, \\
b_2 =&(B1(\Delta X_{14}\Delta Z_{13} - \Delta X_{13}\Delta Z_{14}) + B2(\Delta X_{12}\Delta Z_{14} - \Delta X_{14}\Delta Z_{12}) \\
&+ B3(\Delta X_{13}\Delta Z_{12} - \Delta X_{12}\Delta Z_{13}))/d, \\
b_3 =&(B1(\Delta X_{13}\Delta Y_{14} - \Delta X_{14}\Delta Y_{13}) + B2(\Delta X_{14}\Delta Y_{12} - \Delta X_{12}\Delta Y_{14}) \\
&+ B3(\Delta X_{12}\Delta Y_{13} - \Delta X_{13}\Delta Y_{12}))/d,
\end{aligned} \tag{A.12}$$

and the denominator d in the above expressions is:

$$\begin{aligned}
d =& - \Delta X_{14}\Delta Y_{13}\Delta Z_{12} + \Delta X_{13}\Delta Y_{14}\Delta Z_{12} + \Delta X_{14}\Delta Y_{12}\Delta Z_{13} \\
&- \Delta X_{12}\Delta Y_{14}\Delta Z_{13} - \Delta X_{13}\Delta Y_{12}\Delta Z_{14} + \Delta X_{12}\Delta Y_{13}\Delta Z_{14}.
\end{aligned} \tag{A.13}$$

Once x, y and z as functions of t are obtained as in equation (A.10), their insertion into any of the initial equations (let us choose (A.1)) yields a quadratic equation with t as the only unknown:

$$(a_1 t + b_1 - X_1)^2 + (a_2 t + b_2 - Y_1)^2 + (a_3 t + b_3 - Z_1)^2 = c^2(t - T_1)^2. \tag{A.14}$$

The above equation may be transformed to the general form:

$$pt^2 + qt + r = 0, \tag{A.15}$$

with the p, q, r coefficients expressed with the previously introduced terms as:

$$\begin{aligned}
p &= a_1^2 + a_2^2 + a_3^2 - c^2, \\
q &= 2a_1(b_1 - X_1) + 2a_2(b_2 - Y_1) + 2a_3(b_3 - Z_1) + c^2 T_1, \\
r &= (b_1 - X_1)^2 + (b_2 - Y_1)^2 + (b_3 - Z_1)^2 - c^2 {T_1}^2.
\end{aligned} \tag{A.16}$$

Equation (A.15) has up to two solutions which in this work are labeled t_1 and t_2 as below:

$$t_1 = \frac{-q - \sqrt{q^2 - 4pr}}{2p}, \qquad t_2 = \frac{-q + \sqrt{q^2 - 4pr}}{2p}. \tag{A.17}$$

Although from the mathematical point of view it is possible that no solutions exist if $q^2 < 4pr$, it should not be the case when the data from a physical event are used where

the real vertex corresponding to a solution always exists[1]. It may be, however, that both solutions are equivalent, i.e. $t_1 = t_2$.

Finally, insertion of the explicit solutions for t into equation (A.10) leads to the full solutions of the initial system composed of kaon flight time t and the spatial decay vertex coordinates x, y, z:

$$\begin{aligned} &(t_1, x(t_1), y(t_1), z(t_1)) \\ &(t_2, x(t_2), y(t_2), z(t_2)) \end{aligned} \tag{A.18}$$

[1] Reconstruction effects, however, can make this equation unsolvable.

Bibliography

[1] G. Rochester and C. Butler, "Evidence for the existence of new unstable elementary particles," *Nature* **160** (1947) 855–857.

[2] J. Christenson, J. Cronin, V. Fitch, and R. Turlay, "Evidence for the 2 pi Decay of the k(2)0 Meson," *Phys. Rev. Lett.* **13** (1964) 138–140.

[3] A. Sergi, "Recent results from Kaon Physics,"(2013) `arXiv:1303.0629 [hep-ex]`.

[4] A. Einstein, B. Podolsky, and N. Rosen, "Can quantum mechanical description of physical reality be considered complete?," *Phys. Rev.* **47** (1935) 777–780.

[5] Particle Data Group Collaboration, J. Beringer *et al.*, "Review of Particle Physics (RPP)," *Phys. Rev.* **D86** (2012) 010001.

[6] A. Di Domenico, "Handbook on neutral kaon interferometry at a Phi-factory," *Frascati Physics Series* **43** (2007) 1–38.

[7] G. D'Ambrosio, G. Isidori, and A. Pugliese, "CP and CPT measurements at DAPHNE," in *The second DAPHNE physics handbook*, L. Maiani, G. Pancheri, and N. Paver, eds., vol. 1 (1995) 63–95. `arXiv:hep-ph/9411389 [hep-ph]`.

[8] I. Balwierz, "Measurement of the neutral kaon regeneration cross-section in beryllium at P=110 MeV/c with the KLOE detector," Master thesis, Jagiellonian University (2011). `http://koza.if.uj.edu.pl/files/5275c8710f8aa6928cbe3f0dd4b676c8/Balwierz_Izabela_master_thesis.pdf`.

[9] L. Ametller, "Electromagnetic eta decays," in *The second DAPHNE physics handbook*, L. Maiani, G. Pancheri, and N. Paver, eds., vol. 1 (1997) 427–444.

[10] E. Shabalin, "Weak decays of eta mesons," in *The second DAPHNE physics handbook*, L. Maiani, G. Pancheri, and N. Paver, eds., vol. 1 (1997) 445–448.

[11] S. Giovannella, "U boson searches at KLOE," *J. Phys. Conf. Ser.* **335** (2011) 012067, `arXiv:1107.2531 [hep-ex]`.

[12] K. Kleinknecht, "Results on rare decays of neutral kaons from the NA31 experiment at CERN," *Frascati Physics Series* **3** (1994) 377–398.

[13] NA48/2 and NA62 Collaboration, A. Winhart, "Kaon physics at CERN: Recent results from the NA48/2 and NA62 experiments," *EPJ Web Conf.* **37** (2012) 01010.

[14] R. Wanke, "New results in kaon physics from NA48 and KTeV," *eConf* **C030626** (2003) FRAT07, arXiv:hep-ex/0309078 [hep-ex].

[15] C. Buchanan, R. Cousins, C. Dib, R. Peccei, and J. Quackenbush, "Testing CP and CPT violation in the neutral kaon system at a phi factory," *Phys. Rev.* **D45** (1992) 4088–4107.

[16] M. Ciuchini, E. Franco, G. Martinelli, and L. Reina, "Estimates of epsilon-prime / epsilon," in *The second DAPHNE physics handbook*, L. Maiani, G. Pancheri, and N. Paver, eds., vol. 1 (1995) 27–50. arXiv:hep-ph/9503277 [hep-ph].

[17] M. Hayakawa and A. Sanda, "Searching for T, CP, CPT and Delta S = Delta Q rule violations in the neutral K meson system: A Guide," *Phys. Rev.* **D48** (1993) 1150–1166, arXiv:hep-ph/9302206 [hep-ph].

[18] G. D'Ambrosio and G. Isidori, "CP violation in kaon decays," *Int. J. Mod. Phys.* **A13** (1998) 1–94, arXiv:hep-ph/9611284 [hep-ph].

[19] M. Sozzi, "On the direct CP violation parameter epsilon-prime," *Eur. Phys. J.* **C36** (2004) 37–42, arXiv:hep-ph/0401176 [hep-ph].

[20] A. Pais and O. Piccioni, "Note on the decay and absorption of the θ^0," *Phys. Rev.* **100** (1955) 1487–1489.

[21] R. Good, R. Matsen, F. Muller, O. Piccioni, W. Powell, *et al.*, "Regeneration of neutral k mesons and their mass difference," *Phys. Rev.* **124** (1961) 1223–1239.

[22] F. Ceradini, A. Di Domenico, and A. Ferrari, "Measurement of neutral kaon regeneration cross sections in the first months of kloe data taking." KLOE Memo N.169/98 (1998).

[23] G. Vignola, M. Bassetti, M. Biagini, C. Biscari, R. Boni, *et al.*, "DAPHNE, the first Phi-factory," *Conf. Proc.* **C960610** (1996) 22–26.

[24] KLOE Collaboration, F. Bossi, E. De Lucia, J. Lee-Franzini, S. Miscetti, and M. Palutan, "Precision Kaon and Hadron Physics with KLOE," *Riv. Nuovo Cim.* **31** (2008) 531–623, arXiv:0811.1929 [hep-ex].

[25] M. Zobov, D. Alesini, M. Biagini, C. Biscari, A. Bocci, *et al.*, "Test of crab-waist collisions at DAFNE Phi factory," *Phys. Rev. Lett.* **104** (2010) 174801.

[26] M. Adinolfi, F. Ambrosino, M. Antonelli, C. Bini, V. Bocci, *et al.*, "The QCAL tile calorimeter of KLOE," *Nucl.Instrum.Meth.* **A483** (2002) 649–659.

[27] J. Lee-Franzini and P. Franzini, "A Flavor of KLOE," *Acta Phys. Polon.* **B38** (2007) 2703–2730, arXiv:hep-ex/0702016 [hep-ex].

[28] *The KLOE experiment web site* . http://www.lnf.infn.it/kloe. [Online; accessed 25-april-2013].

[29] M. Adinolfi, F. Ambrosino, A. Andryakov, A. Antonelli, M. Antonelli, *et al.*, "The tracking detector of the KLOE experiment," *Nucl. Instrum. Meth.* **A488** (2002) 51–73.

[30] M. Adinolfi, F. Ambrosino, A. Antonelli, M. Antonelli, F. Anulli, *et al.*, "The KLOE electromagnetic calorimeter," *Nucl. Instrum. Meth.* **A482** (2002) 364–386.

[31] B. Di Micco, "Kloe calorimeter," Presented at the 10-th International Conference On Instrumentation For Colliding Beam Physics, Budker Institute of Nuclear Physics, Novosibirsk (2008).

[32] J. Zdebik, "Merging and splitting of clusters in the electromagnetic calorimeter of the KLOE detector," Master thesis, Jagiellonian University (2008). `arXiv:0811.1377 [physics.ins-det]`.

[33] F. Ambrosino, A. Antonelli, M. Antonelli, C. Bini, C. Bloise, *et al.*, "Data handling, reconstruction, and simulation for the KLOE experiment," *Nucl. Instrum. Meth.* **A534** (2004) 403–433, `arXiv:physics/0404100 [physics]`.

[34] S. Bocchetta Master thesis, Universita Di Roma Tre (2006).

[35] CMD-2 Collaboration, E. Solodov, "Study of the rare K^0(S), K^0(L), K^+, K^- decays at ϕ resonance with the CMD-2 detector,". Proceedings at 29th International Conference on High-Energy Physics (ICHEP 98), World Scientific (1998).

[36] KLOE Collaboration, F. Ambrosino *et al.*, "First observation of quantum interference in the process $\phi \to K_S K_L \to \pi^+\pi^-\pi^+\pi^-$: A Test of quantum mechanics and CPT symmetry," *Phys. Lett.* **B642** (2006) 315–321, `arXiv:hep-ex/0607027 [hep-ex]`.

[37] G. Lanfranchi, "Direct measurement of the K_L lifetime." KLOE Memo N.296/04 (2004).

[38] F. James and M. Roos, "Minuit: A System for Function Minimization and Analysis of the Parameter Errors and Correlations," *Comput.Phys.Commun.* **10** (1975) 343–367.

[39] N. Gould, "Penalty and augmented Lagrangian methods in equality constrained optimization." [Online; accessed 2-june-2013].